



UNIVERSITY OF THESSALY

THESIS

---

**Cryogenic Semiconductor Detectors:  
Simulation of Signal Formation &  
Irradiation Beam Test**

---

*Author:*  
Andreas ALEXOPOULOS

*Supervisors:*  
Dr. Mariusz SAPINSKI  
Dr. Georgios STAMOULIS  
Dr. Dionisis VAVOUGIOS



Geneva, September 21, 2015



# Abstract

The Beam Loss Monitoring system of the Large Hadron Collider is responsible for the protection of the machine from damage and for the prevention of a magnet quench. Near the interaction points of the LHC, in the triplet magnets area, the BLMs are sensitive to the collision debris, limiting their ability to distinguish beam loss signal from signal caused due to the collision products. Placing silicon & diamond detectors inside the cold mass of the magnets, in liquid helium temperatures, would provide significant improvement to the precision of the measurement of the energy deposition in the superconducting coil of the magnet.

To further study the signal formation and the shape of the transient current pulses of the aforementioned detectors in cryogenic temperatures, a simulation application has been developed. The application provides a fast way of determining the electric field components inside the detectors bulk and then introduces an initial charge distribution based on the properties of the radiation. Subsequently, charge transport and trapping phenomena are being simulated and the final induced current is calculated based on the Shockley-Ramo theorem.

Finally, to test the radiation hardness of the silicon and diamond detectors, an irradiation test has been conducted on the IRRAD facility of the PS East Area. The irradiated samples were two silicon pad diodes with thickness of  $100\text{ }\mu\text{m}$  &  $300\text{ }\mu\text{m}$ , a  $300\text{ }\mu\text{m}$  3D silicon and a  $500\text{ }\mu\text{m}$  3D single-crystal diamond. For that purpose, an client application for the BLEDP stand-alone data acquisition system has been developed. The application has been designed to collect, store, display and additionally do offline analysis on the acquired data. After the completion of the test, approximately 28.000 signals have been recorder for each device reaching a maximum fluence of  $2.834 \cdot 10^{15}$  protons/cm<sup>2</sup>. The collected data provide useful information on the detectors signal response and charge collection efficiency degradation presented in this work and form a solid base for further investigation.





# Περίληψη

Το σύστημα παρακολούθησης της δέσμης (BLM) του Large Hadron Collider (LHC) είναι υπεύθυνο για την προστασία του επιταχυντή από βλάβες και για την πρόληψη της μετάστασης κάποιου μαγνήτη από υπεραγώγιμη σε αγώγιμη κατάσταση. Κοντά στα σημεία σύγκρουσης του LHC, στην περιοχή της εσωτερικής τριπλέτας, οι αισθητήρες του BLM είναι ευαίσθητοι στα θραύσματα της σύγκρουσης, περιορίζοντας την ικανότητά τους να διαχωρίσουν σήμα λόγω απώλειας δέσμης από την διέγερση που προκλήθηκε λόγω των προϊόντων της σύγκρουσης. Τοποθετώντας αισθητήρες πυριτίου και διαμαντιού μέσα στην κρύα μάζα του μαγνήτη, σε θερμοκρασίες υγρού ηλίου, θα παρείχε ακριβέστερη μέτρηση της ενέργειας που απορροφάται από το υπεραγώγιμο ηνίο του μαγνήτη.

Για την περαιτέρω μελέτη της διαμόρφωσης του σήματος και του σχήματος του παλμού ρεύματος των προαναφερθέντων ανιχνευτών σε κρυογονικές θερμοκρασίες, υλοποιήθηκε μία εφαρμογή εξομοίωσης. Η εφαρμογή παρέχει ένα γρήγορο τρόπο καθορισμού του ηλεκτρικού πεδίου στους ανιχνευτές και στη συνέχεια εισάγει μία αρχική κατανομή του διεγερμένου φορτίου, βάσει των ιδιοτήτων της πηγής ακτινοβολίας. Ακολουθώντας, εξομοιώνεται η κίνηση και παγίδευση των φορτίων μέσα στον ανιχνευτή και το τελικό επαγόμενο ρεύμα υπολογίζεται βάσει του θεωρήματος Shockley-Ramo.

Τέλος, για την δοκιμή των ανιχνευτών σε συνθήκες ακτινοβολίας, διεξήχθη ένα πείραμα στις εγκαταστάσεις IRRAD της ανατολικής πτέρυγας του PS . Τα δείγματα προς δοκιμή ήταν δύο επίπεδες δίοδοι πυριτίου πάχους 100  $\mu\text{m}$  και 300  $\mu\text{m}$ , ένας ανιχνευτής πυριτίου 300  $\mu\text{m}$  3D δομής, και ένας ανιχνευτής διαμαντιού 500  $\mu\text{m}$  επίσης 3D δομής. Για αυτό το σκοπό, αναπτύχθηκε μία εφαρμογή πελάτη για το BLEDP αυτόνομο σύστημα περισυλλογής δεδομένων. Η εφαρμογή σχεδιάστηκε για να συλλέγει, αποθηκεύει, απεικονίζει αλλά και να κάνει offline ανάλυση στα ληφθέντα δεδομένα. Με την ολοκλήρωση της δοκιμής, περίπου 28.000 σήματα συλλέχθηκαν για κάθε ανιχνευτή, φθάνοντας μέγιστη απορροφούμενη δόση  $2.834 \cdot 10^{15}$  protons/cm<sup>2</sup>. Τα συλλεχθέντα δεδομένα παρέχουν χρήσιμες πληροφορίες για την απόκριση του σήματος και την υποβάθμιση της αποδοτικότητας συλλογής φορτίου των ανιχνευτών, οι οποίες παρουσιάζονται στην εργασία αυτή, και αποτελούν στέρεα βάση για περαιτέρω έρευνα.



# Acknowledgements

My experience at CERN has been an unprecedented and unique period of my life. I had the luck and honour to work with and benefit from some extraordinary people. Expressing my gratitude to all those people in a single page feels impossible, but I would hereby like to make an effort.

First and foremost, I would like to express my gratitude to my supervisor **Mariusz Sapinski** for trusting me and providing me the possibility to start this journey. He has been of great support throughout all the difficulties we encountered, giving me directions and incentives to work and research more. His guidance and comments have been of great value for me and for my thesis. I would also like to deeply thank **Bernd Dehning** for all his advice and feedback. He was very interested in the projects progress, and without his counsel and contribution this work would definitely not have been the same.

Undoubtedly, I am very obliged to all of the staff of BE-BI-BL section and I would like to mention just a few. First, I would like to thank **Marcin Bartosik** for his collaboration regarding the project. We have shared a lot of work in the LHC and he had a key-role for the successful completion of the irradiation test. **Christos Zamantzas**, **William Vigano** and **Maciej Kwiatkowski** have been of great help, providing the equipment and information over the operation and specification of the BLEDP stand-alone DAQ system. I highly appreciate the time **Emiliano Piselli** dedicated to the design of the LabView program dedicated to the pressure and temperature monitoring of the cryostat. **Jose Luis Sirvent Blasco** has given me necessary directions in the development of a control application of the Keithley instruments through GPIB. I could not forget to mention **Maria Kastriotou**, **Plamen Hopchev**, **Roberto Rocca** and **Athanasios Topaloudis** for all the conversations we had over a wide variety of subjects of our common interest. Last but not least, I want to thank my friend & colleague **Matteo Macchini**, with whom being in the same office has been a joy and a continuous exchange of useful information.

Moreover, **Vladimir Eremin** and **Elena Verbitskaya** from Ioffe Institute have been of great support, providing the two Si pad detectors for the irradiation test and analysing the results. Similarly, the other two 3D detectors were kindly provided by **Alexander Oh** and **Giulio Forcolin** from Manchester University, to whom I am thankful also for our discussions on the ongoing analysis. **Federico Ravotti**, **Maurice Glaser** and **Blerina Gotse** have greatly contributed in this work by sharing the collected data from their BPMs.

Furthermore, I would like to acknowledge my supervisors in the University of Thessaly, **Georgios Stamoulis** and **Dionisis Vavougiou** who undertook the difficult task of supervising a student from a distance and supporting my career path. Also, I could not forget to thank my professors **Ioannis Katsavounidis** and **Elias Houstis** for the knowledge and inspiration I gained through their courses and their valuable help in every case needed.

Finally, there are some people that have always been by my side, believing in me and supporting me under any circumstances. I would like to thank my friends for always being close to me despite the time we spend apart. Also, my family have always provided their unlimited love and care, helping me form a solid ground for my personality and education. Last, a special thank you towards Nadia, with whom I have shared everything for the last 10 years and who is the reason of my happiness and fulfilment.



# Abbreviations

BLEDP:	Beam Loss Emissions Dual Polarity
BLM:	Beam Loss Monitor
BPM:	Beam Position Monitor
CCD:	Charge Collection Distance
CCE:	Charge Collection Efficiency
CERN:	European Organization for Nuclear Research
CFC:	Current-to-Frequency Converter
CID:	Current Injected Detector
CSV:	Comma Separated Values
CryoBLM:	Cryogenic Beam Loss Monitor
DADC:	Direct Analog Digital Converter
FDFC:	Fully Differential Frequency Converter
FWHM:	Full Width Half Maximum
FPGA:	Field Programmable Gate Array
GUI:	Graphical User Interface
HEP:	High Energy Physics
IP:	Internet Protocol
LHC:	Large Hadron Collider
LHe:	Liquid Helium
MFP:	Mean Free Path
MIP:	Minimum Ionizing Particle
MPS:	Machine Protection System
MTU:	Maximum Transmission Unit
NIEL:	Non Ionizing Energy Loss
PDF:	Probability Density Function
PS:	Proton Synchrotron
RMS:	Root Mean Square
RT:	Room Temperature
sCVD:	Single Crystal Chemical Vapor Deposition diamond detector
SEC:	Secondary Emission Chamber
Si:	Silicon detector
SMA:	Simple Moving Average
SNR:	Signal-to-Noise Ratio
SPS:	Super Proton Synchrotron
TCP:	Transmission Control Protocol
TCT:	Transient Current Technique
UDP:	User Datagram Protocol



# Contents

<b>1</b>	<b>Introduction</b>	<b>1</b>
1.1	About CERN . . . . .	1
1.2	The CERN Accelerator Complex . . . . .	2
1.3	Beam Instrumentation & Beam Loss Monitoring . . . . .	5
1.4	Chapters review . . . . .	6
<b>2</b>	<b>The Cryogenic BLM project</b>	<b>7</b>
2.1	The Beam Loss Monitoring System . . . . .	7
2.1.1	The BLM Detectors . . . . .	8
2.1.2	Beam Loss Scenarios . . . . .	11
2.1.3	The limits of the present BLM system . . . . .	11
2.1.4	Silicon & Diamond CryoBLMs . . . . .	13
<b>3</b>	<b>Physics of Semiconductor Detectors</b>	<b>15</b>
3.1	Radiation Detection . . . . .	15
3.1.1	Minimum Ionizing Particles . . . . .	18
3.1.2	$\alpha$ -particles . . . . .	19
3.1.3	Photons . . . . .	20
3.2	Semiconductor Detectors . . . . .	22
3.2.1	Depletion Region . . . . .	24
3.2.2	Drift Velocity of carriers . . . . .	24
3.2.3	Weighting & Electric Field . . . . .	25
3.2.4	Charge carrier mobility . . . . .	26
3.2.5	Saturation Velocity . . . . .	27
3.2.6	Shockley-Ramo theorem . . . . .	28
3.3	Radiation Damage . . . . .	29

## CONTENTS

---

3.3.1	Effects of radiation damage on detectors . . . . .	30
<b>4</b>	<b>The Transient Current Technique &amp; Simulation</b>	<b>34</b>
4.1	The Transient Current Technique . . . . .	34
4.2	TCT Simulation Application . . . . .	36
4.2.1	Pulse Shaping Algorithm . . . . .	37
4.2.2	Software Description . . . . .	38
4.3	Conclusions and Future Suggestions . . . . .	44
<b>5</b>	<b>Cryogenic Irradiation Experiment</b>	<b>45</b>
5.1	Introduction . . . . .	45
5.2	The BLEDP stand-alone acquisition system . . . . .	49
5.2.1	The BLEDP Card . . . . .	49
5.2.2	BLEDP Communication Protocol . . . . .	50
5.2.3	Data Acquisition Application . . . . .	51
5.3	Data Analysis . . . . .	58
5.4	Conclusions and Future Suggestions . . . . .	67
<b>6</b>	<b>Conclusions</b>	<b>68</b>



# Introduction

## 1.1 About CERN

The European Organization for Nuclear Research (CERN) is a European research organization founded in 1954 that operates the largest particle physics laboratory in the world. The CERN laboratory is located at the Franco-Swiss border near Geneva and as of June 2015 CERN has 22 countries registered as full members (Figure 1.1). It is affiliated with over 600 universities and institutions from all over the world resulting in over 10.000 working scientists of over 100 different nationalities. CERN's main function is to provide the particle accelerators and other infrastructure so that high-energy physics (HEP) research can be performed.

The main field of research of CERN is particle physics and physicists and engineers are probing the fundamental structure of the universe and studying the basic constituents of matter - the fundamental particles. Since its foundation several discoveries have been made including the the W and Z boson discovery (1983, UA1 & UA2 experiments) using the SPS, the discovery of CP (charge parity) violation again in SPS (1999, NA48 experiment) and several achievements related to antimatter, with the creation, isolation and maintenance of antihydrogen. More recently, using the LHC, CERN has been awarded with the discovery of a boson of mass  $\sim 125 \text{ GeV}/c^2$ , consistent with the long-sought *Higgs boson*. In addition to the above, several other technological developments have been achieved at CERN. The World Wide Web began as a CERN project under the name ENQUIRE for the facilitation of information sharing among physicists. Moreover, over the last years, CERN has become a pioneer in the developments in the area of grid computing, hosting projects including the *Enabling Grids for E-science* (EGEE). CERN has been also contributing significant research to areas such as cryogenics, superconductivity and vacuum as LHC is the largest operational system



Figure 1.1: CERN's logo and member states as of June 2015.

in the world using the aforementioned technologies. Finally, medical applications such as cancer treatment and medical imaging have benefited greatly of CERN's know-how in accelerators, industrial imaging and radiation protection.

### 1.2 The CERN Accelerator Complex

The instruments used at CERN are particle accelerators and detectors. Accelerators boost beams of particles to very high energy and to almost the speed of light before colliding them with each other or with stationary targets. Detectors are assigned to monitor, observe and record the operation and results of these activities.

The accelerator complex at CERN is a succession of linear or circular accelerators designed to accelerate protons or lead ions to high energies (Figure 1.2 ). Most accelerators have their own experimental halls where beams are used for experiments at lower energies. Each accelerator increases the beams energy before injecting the beam to the next accelerator in the chain.

Two different particles types, protons and lead ions, are accelerated through CERN's accelerator complex. Protons are provided from a simple compressed gas hydrogen bottle, after stripping orbiting electrons by a magnetic field to isolate the hydrogen nuclei. Then, these protons are accelerated in the linear accelerator LINAC2 to energies

## 1.2. THE CERN ACCELERATOR COMPLEX

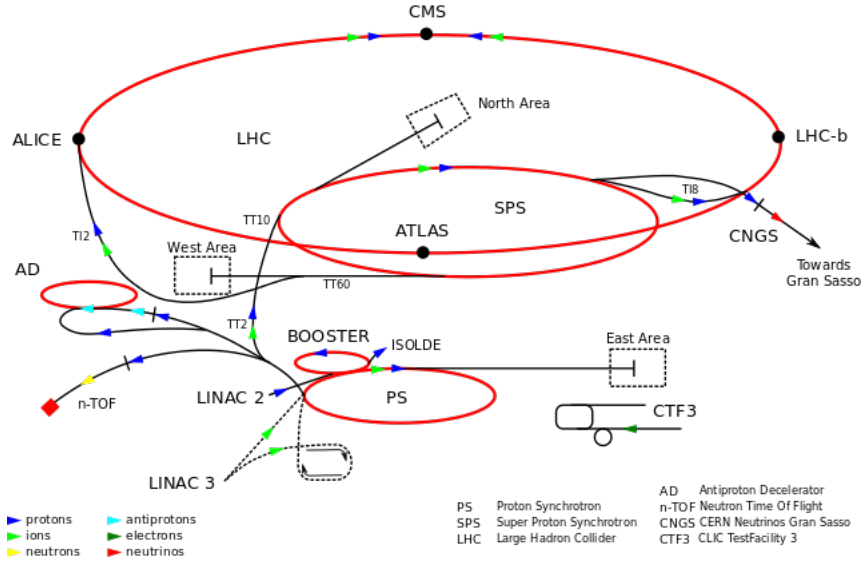


Figure 1.2: CERN's Accelerator Complex.

up to 50 MeV and speed equal to a third of speed of light. Subsequently, the proton beam is injected to the PS Booster, a circular accelerator of circumference of 157 m, where the beam is separated to 4 different bunches in order to maximize its intensity. The bunches are accelerated by repeatedly circulating the Booster while being under the influence of a synchronized pulsed electric field. Before leaving the Booster, the protons are accelerated to 1.4 GeV and 91.6% the speed of light. Lead ions are following a different but similar course, first created from vaporized lead ionized by an electron current. Various states are produced with a maximum around  $Pb^{29+}$  which then is accelerated by LINAC3 to energies up to 4.2 MeV/u (energy per nucleon). The beam passes through a carbon foil which strips most of them to  $Pb^{54+}$  before passing to the Low Energy Ring (LEIR). The LEIR takes the task of splitting the beam into 4 bunches and accelerates them to 72 MeV/u in about 2.5 seconds. Afterwards, both types of particles are following the same course, starting with the injection to the Proton Synchrotron (PS).

The PS is the oldest circular accelerator, first commissioned in 1959 being CERN's flagship accelerator and world's highest energy particle accelerator at that time. With a circumference of 628 m, the PS has 277 conventional electromagnets from which 100 are dipoles tasked to bend the beam to its circular trajectory. Throughout its operation, PS has accelerated various particles including  $\alpha$ -particles (helium nuclei), oxygen and sulphur nuclei, electrons, positrons and antiprotons in addition to protons and lead ions

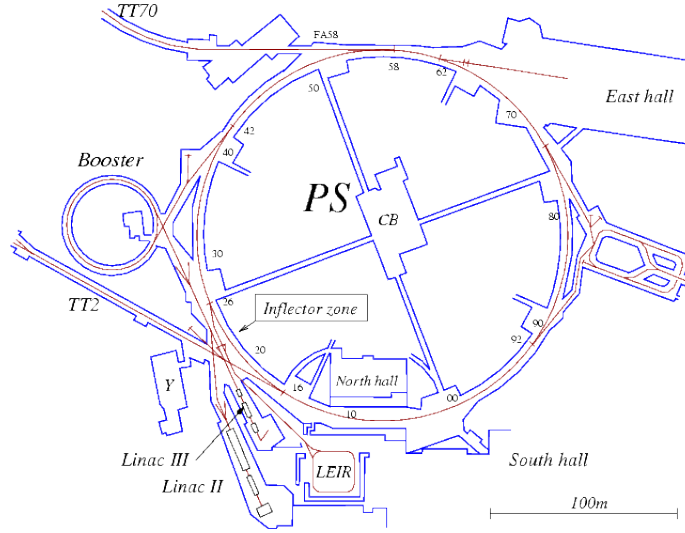


Figure 1.3: The Proton Synchrotron Complex.

which is currently accelerating. Protons are accelerated up to 25 GeV and 99.93% the velocity of light and lead ions to 5.9 GeV/u. Lead ions are in addition directed through another carbon foil which strips the heavy ions to  $Pb^{82+}$ . At this point, as the particles cannot be accelerated beyond the speed of light, increased energy is seen increase of their (relativistic) mass. As a result, the mass of a rotating proton is  $\sim 26.73$  times larger than its rest mass. It is worth mentioning, especially in the context of this work, that the PS is providing particles to various Secondary Beams & Areas (SBA) (Figure 1.3), one of which being the East Area.

After the PS, the particle beam is inserted to the Super Proton Synchrotron (SPS), CERN's second largest accelerator. The SPS is nearly 7 km long in circumference and consists of 1317 conventional electromagnets, 744 of which are dipoles. Protons are accelerated from the SPS up to energies of 450 GeV and lead ions to 177 GeV/u. Now protons are rotating at 99.9998% the speed of light and weight  $\sim 500$  times their rest mass. At the final stage, the SPS injects the particle beam in the Large Hadron Collider in two opposite directions. The LHC sits below the earth's surface in depth varying from 50 m to 175 m and is the worlds largest particle collider with a circumference of  $\sim 27$  km. The machine uses a variety of magnets, totalling to almost 9600, 1232 of which being the main dipoles. In order to achieve the magnetic fields required to manage the particle beam (peak  $\sim 8$  T), most of LHC magnets are superconducting and therefore cooled by worlds largest cryogenic system. During the first run of the LHC (2010-2013), protons were accelerated up to 3.5 TeV per beam resulting in a

collision energy of 7 TeV. After a two year shut-down of the machine for maintenance and upgrades, the LHC restarted in April of 2015 achieving to circulate proton beams of 6.5 TeV energy for a total collision energy of 13 TeV.

The aforementioned accelerators are providing particles to various different experiments which ensure that a wide range of physics research is covered at CERN. In brief, ATLAS and CMS detectors of LHC have been in the center of attention due to the greatly appreciated Higgs boson discovery. Also using LHC beams, ALICE is a detector dedicated to the lead ion program, while LHCb mainly concentrates on CP violation in the b-quark system. While the main focus of research at CERN has moved towards LHC, experiments at other accelerators also remain of great importance and active research. Epigrammatically mentioning only a few, SPS is providing beams the Common Muon and Proton Apparatus for Structure and Spectroscopy (COMPASS) fixed target experiment, PS supplies the Cosmics Leaving Outdoor Droplets (CLOUD) experiments, PSB feeds the Isotope mass Separator On-Line (ISOLDE) facility while Antihydrogen Trap (ATRAP) uses protons from AD.

## 1.3 Beam Instrumentation & Beam Loss Monitoring

Beam instrumentation relates to the design, construction, maintenance and operation of the instruments that allow the scientists to observe the particle beams and to measure related parameters for CERN's accelerators and transfer lines. The CERN group assigned to the task is engaged in research and development for the improvement of existing detection techniques and the exploration of new methods which will allow the optimization of the machines operation for current and future challenges. The activities of the group ranges from accelerator physics and detector technologies to custom built electronics and software. The parameters of interest for beam instrumentation are the beam's position in both horizontal and vertical axes and its profile in terms of transverse and longitudinal intensity distribution. Moreover, beam intensity should be measured both with charge bunch-by-bunch measurement techniques and total circulating current outputs while beam's luminosity maximisation is the goal of all optimisations using the beam parameter knowledge. Last but not least, beam loss refers to the energy deposition of particles diverging from the desired trajectory and impacting LHC material, which is of great significance for machine protection, especially in the case of superconducting magnets.

The LHC beam loss monitor system is part of the LHC's machine protection system (MPS). Its role includes the protection of the machine from damage or the prevention of beam-loss induced magnet quench, that is the transition of a magnet from super

to normal conducting state, by triggering a beam dump. A magnet quench results in several hours of downtime, while in the worst case of machine damage the results could end in months of downtime and significant cost. It is therefore evident that such a system must have a very high level of reliability, requiring redundancy of high quality and radiation hard components so that voting techniques can also be applied. On the other hand, the system should not trigger false dumps, minimizing the down-time of the machine and achieving maximum operational efficiency. Furthermore, the BLM system should be fast, meaning that a beam dump signal should be triggered in less than  $89\text{ }\mu\text{s}$ , that is the time needed for a single LHC revolution. It is also apparent that a very important criterion is the determination of the trigger threshold values which is the subject of extensive measurements and simulations. Finally, such a system can also serve as a diagnostics tool for the optimization of the accelerators performance. A more detailed insight to the BLM system will be provided in the next chapter.

### 1.4 Chapters review

In **Chapter 2** The Cryogenic Beam Loss Monitors Project (CryoBLM) is presented, its challenges, conception and necessity as well as previous related works. In **Chapter 3** an overview of the physics of semiconductor detectors is provided, with information related to charge creation, collection and trapping, as later used for the modelling and development of the simulation application. In **Chapter 4** the Transient Current Technique (TCT) is introduced, focusing on the simulation software design and outputs of the TCTsim application. In **Chapter 5** the Cryogenic Irradiation Experiment conducted in December of 2014 is presented along with the purpose-built data acquisition software and the retrieved results. Last, in **Chapter 6** some observations are summarized and conclusions are attempted while also proposing goals and challenges for the future studies.

# The Cryogenic BLM project

## 2.1 The Beam Loss Monitoring System

A great amount of energy is stored in the LHC (Table 2.1) and a loss of even a fraction of that energy may induce a quench on the LHC’s superconducting magnets or even damage any of the machines physical components. Concerning beam loss monitoring, the energy of 362 MJ per circulating beam could affect critically the functionality of the machine. The high intensity and small transverse dimension of the beam result in a beam energy density in the LHC that outreaches other accelerators by a factor of 1000. The energy density is the most relevant parameter for beam-induced damage. As little as 1 mJ/cm<sup>3</sup> can quench a magnet and 1 J/cm<sup>3</sup> causes damage at the LHC nominal beam energy. We can therefore deduct the dynamic range of 10<sup>13</sup> orders of magnitude required for an ideal BLM system. The challenges of the LHC BLM system, also mentioned in the previous chapter are summarized in Table 2.2.

Stored Energy	MJ
In a main dipole circuit	1.100
Of the magnet system	10.000
Per rotating beam	362

Table 2.1: Energy stored in LHC magnets considering operation at nominal beam energy of 7 TeV [8].

In Figure 2.1 an overview of the LHC MPS is displayed. The core of the system is the Beam Interlock System (BIS) which receives signals from the surrounding subsystems, referred as User Systems, and transmits them to the Beam Dumping System (BDS).

## 2. THE CRYOGENIC BLM PROJECT

Challenge	Criterion	Requirement
Reliability	Failure Rate	$10^{-7}$ per hour per channel
Operation Efficiency	# of false dumps	Less than 2 per month
High Dynamic Range	Orders of Magnitude	$10^{13}$
Fast Trigger Generation	Time Elapsed	$< 89 \mu s$ (1 LHC turn)
Quench Threshold Calibration	Uncertainty	Factor of 2

Table 2.2: Challenges of the LHC BLM system.

The User Systems are assigned to detect non-nominal machine conditions which would endanger the machine operation, thus requesting a beam dump. In total more than 20.000 channels are coming from approximately 250 user input connections, from which  $\sim 4000$  are part of the BLM system, therefore making it one of the largest systems. All these channels are automatically and continuously checked for being online through the introduction of a very small modulated current which then should be detected.

Depending on the loss duration different subsystems are engaged to protect the machine. Ultra-fast losses mainly refer to instantaneous losses during the injection phase. It is possible that an error could occur in the setting of the beam trajectory or due to kicker magnet malfunction, that is the magnet used to redirect the beam from one accelerator to another. In that case, there is no time for any system to react and only passive components can be used to protect the machine, meaning a dump block designed to absorb the beam which does not follow the desired trajectory. In the case of losses lasting 2–3 turns (fast), the only system capable of detecting and reacting in this time frame is the BLM system. The BLM system sends data to the systems above in the hierarchy twice per beam revolution through an optical link and triggers the BDS with the exclusive use of hardware components. The procedure ends when the next abort gap is encountered and the kicker magnets eject the beam. The procedure takes in total less than 4 LHC turns ( $356 \mu s$ ). As previously mentioned, it was required from the MPS of the LHC to have redundancy for maximum reliability. Hence, following the BLM system, a Quench Protection System (QPS) additionally exists. The QPS does not prevent the quench of a super conducting magnet, but ensures that the magnet will not be damaged by deviating the current from the magnet during the quench. In Figure 2.2 a graphical representation of the above information is presented.

### 2.1.1 The BLM Detectors

The current BLM system consists of three types of detectors, the Ionization Chamber (IC), the Secondary Emissions Monitors (SEM) and the Little Ionization Chamber



## 2.1. THE BEAM LOSS MONITORING SYSTEM

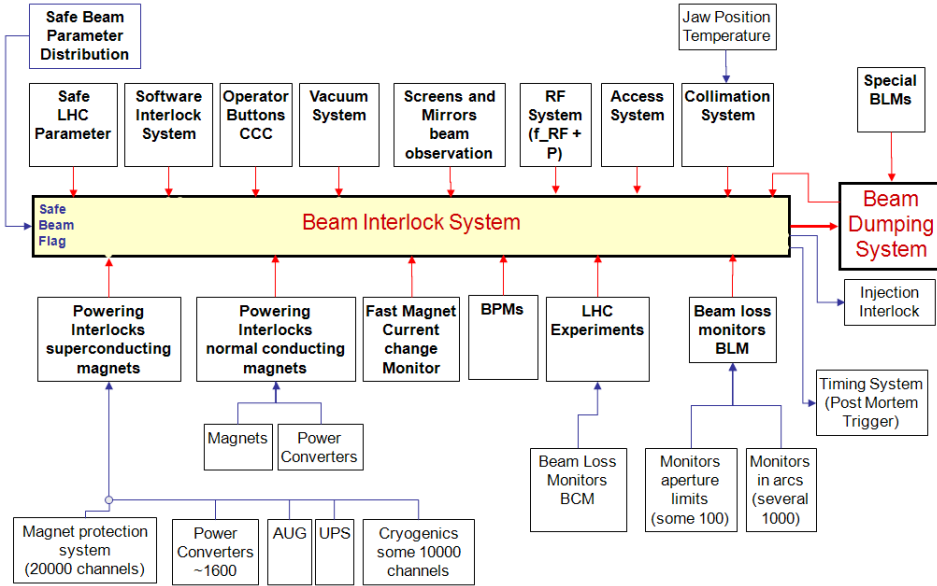


Figure 2.1: An overview of the LHC MPS. Each subsystem can request beam dump through the BIS. Almost 4000 devices are installed as part of the BLM system. The BLM system is the only system to prevent magnet quenches and the main system to prevent magnet damage from multi-turn beam losses.

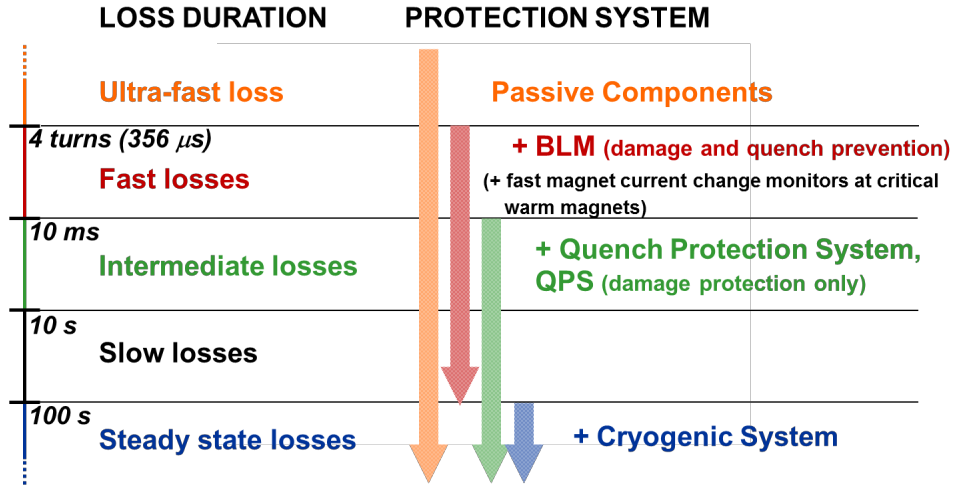


Figure 2.2: A description of the relation between the protection system engagement and the duration of the beam losses.

## 2. THE CRYOGENIC BLM PROJECT

---

(LIC).

The Ionization Chambers (IC), depicted in Figure 2.3, are the standard BLM detectors of the LHC. They are cylindrical in shape and measure 50 cm in length and 9 cm in diameter. The ICs contain 1.5 l of  $N_2$  gas at 100 mbar overpressure so that air does not come in the case of a leak. The detection principle is that beam particles will traverse the detector ionizing electrons and ions in their path which then will be collected on the detectors electrodes due to the application of a bias voltage, usually at 1.5 kV. The time response of the system is limited by the slower ions mobility, whose collection time is of the order of  $80 \mu s$ . The ICs have been tested for their radiation tolerance, and are guaranteed to work with little gain variation up to 100 MGy, meaning they can withstand 30 years of LHC operation. The dynamic range of the device covers  $10^9$  orders of magnitude ( $\sim 1 \text{ pA} - 10 \text{ mA}$ ), being limited by leakage current through the insulator ceramics on the lower end, and saturation effects on the other end. Approximately 3.600 of such devices are installed in the LHC, each one capable of triggering a beam dump [6],[4].

To increase further the dynamic range of the BLM system, the ICs are complemented by Secondary Emissions Monitors and the Little Ionization Chambers. The SEMs and LICs have similar design, but they are smaller and with a significantly smaller sensitivity. These devices are used only for observation purposes and cannot trigger a beam dump, but with appropriate calibration the dynamic range requirement of  $10^{13}$  can be achieved [4].



Figure 2.3: The Ionization Chambers used for the LHC Beam Loss Monitor system and their position in the quadrupole magnets of the arc [6].

### 2.1.2 Beam Loss Scenarios

Beam losses can be classified into regular and irregular losses, the former occurring during normal LHC operation while the latter is mainly due to malfunctioning of the equipment. Regular losses consist the performance limitations of the machine, causing beam instabilities, reducing the beam lifetime or limiting the accelerators luminosity. On the other hand, irregular losses are impossible to predict and usually are very fast. Generally, beam loss scenarios often dealt with the BLM system include:

- Orbit Bumps, mostly controlled by the LHC's feedback systems
- Leakage from Collimators, debris from collimation areas, where controlled losses which are intended for beam cleaning, could reach the cold magnets
- Unidentified Falling Objects (UFOs),  $\mu\text{m}$  sized dust particles that could appear anywhere in the storage ring causing fast localized beam losses
- Luminosity Debris, close to the inner triples caused by the collisions at the interaction point

### 2.1.3 The limits of the present BLM system

Near the interaction points at the position of the LHC's experiments, four purpose-built magnets are placed on each side. The inner triplet magnets as they are called, are designed to squeeze the beam right before the collision maximizing the luminosity. [5].

With the current BLM configuration at the triplet magnet area, the ability to distinguish between energy deposition in the coil due to beam loss is limited by the collision debris which mask the beam loss signal. As can be observed in Figure 2.4, the signal from these debris, which do not present a danger of a magnet quench, exceeds the signal due to quench-provoking beam loss for many BLMs. This problem could be overcome by implementing "topological thresholds", meaning that the beam threshold for the detectors in the inner triplet magnets would be set by taking certain patterns and loss profiles at several BLMs into account. Such a solution would add a small acceptable delay, but as a general practice applying conditional thresholds on the BLMs is more prone to errors. The simulations performed have focused on the inner triplets, but with the luminosity increase of the HL-LHC similar issues could occur in the collimators area as well. It was therefore decided that a more reliable and precise method should be investigated [5].

## 2. THE CRYOGENIC BLM PROJECT

---

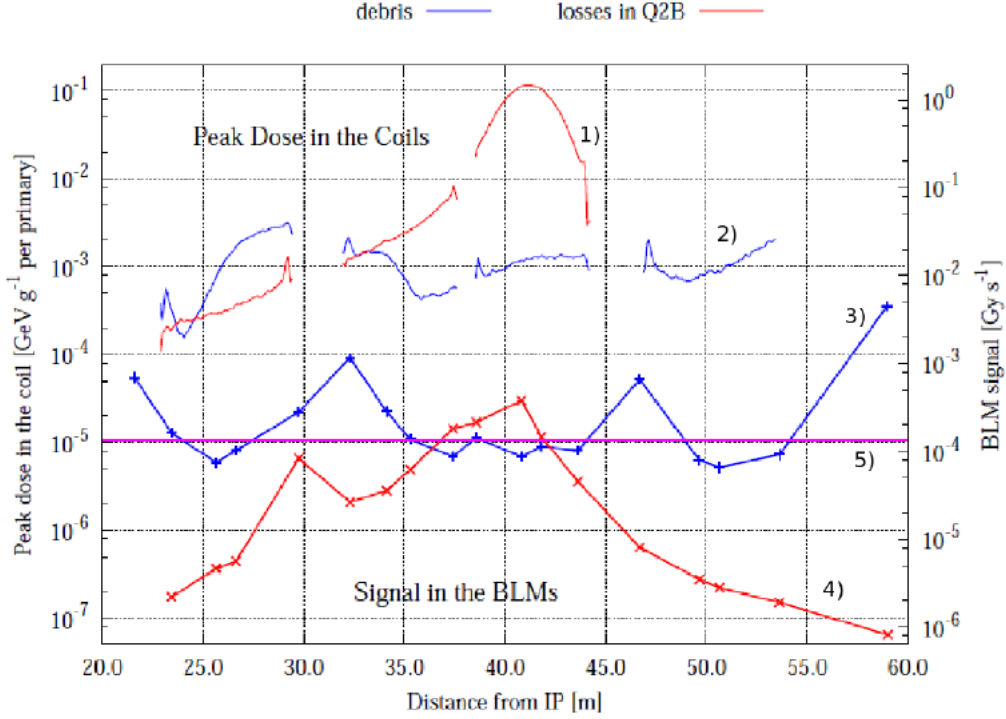


Figure 2.4: 1) Deposited dose in the coils from losses inside the second quadrupole magnet, 2) Deposited dose in the coils from the debris, 3) BLM signal from debris (one cross for each BLM), 4) BLM signal from dangerous losses inside Q2B, 5) Proposed BLM beam abort threshold to protect from dangerous losses. One can see that the debris can mask the signal from a dangerous loss and that the proposed threshold is not adequate [5].

### 2.1.4 Silicon & Diamond CryoBLMs

Previous investigations [5] show that by placing the detectors as close as possible to the superconducting coils one gets a significantly better prevention against beam-induced quenches. Hence, these Cryogenic Beam Loss Monitors (CryoBLMs) should be placed inside the cold mass of the magnet. The requirements for such detectors are the following:

- operation in low temperature of 1.9 K
- radiation tolerance for total integrated dose of 2 MGy in 20 years of LHC operation
- high reliability in magnetic fields of 2 T
- mechanical resistance to pressure rise up from 1.1 to about 20 bar in the case of a magnet quench
- time response faster than 1 ms

Finally, after performed investigations, silicon and diamond detectors have been selected for placement into dipole super conducting magnets for further testing. Diamond detectors have already been used as BLMs (DBLM) for the observation of fast losses with bunch-by-bunch resolution (Figure 2.6), but not in conditions of super-fluid liquid helium temperatures. The placement of the detectors is depicted in Figure 2.5, and has already been applied in cells 9R7 & 9L5 of the LHC. In each magnet 3 silicon and 1 diamond samples have been installed.

In order to investigate the radiation tolerance of silicon and diamond detectors and the degradation of their signal in cryogenic temperatures, irradiation tests have been conducted. The first took place in December 2012 and is covered in detail in [5], while the second performed in December of 2014 is described in this work. Another future test is already planned for November 2015.

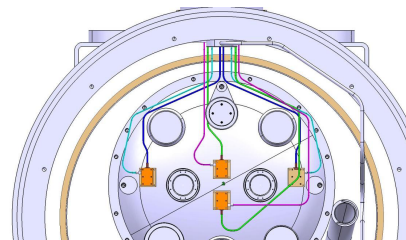


Figure 2.5: Layout of the detectors on the cold mass surface of Main Dipole magnets.[9].

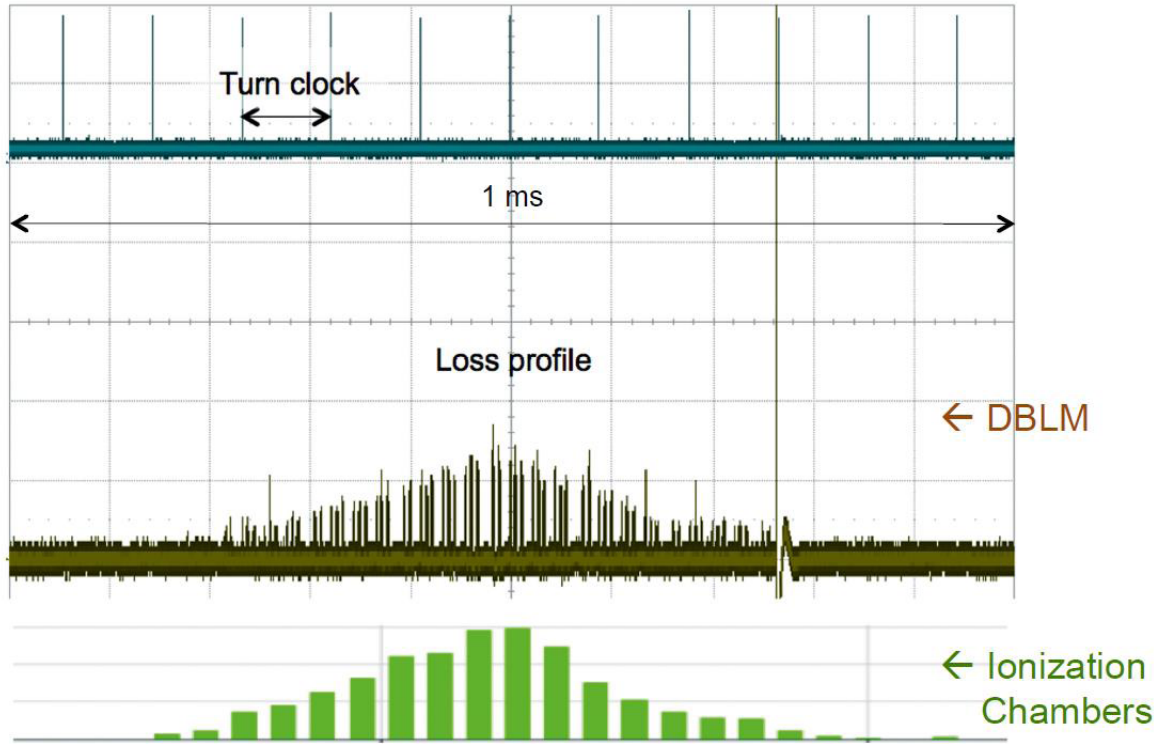


Figure 2.6: A representation of the bunch-by-bunch resolution of a diamond BLM compared to the existing ionization chambers [4].

# Physics of Semiconductor Detectors

## 3.1 Radiation Detection

For the detection of a particle passing through matter, the particle has to deposit energy during its transit and this energy has to be measured. While a charged particle travels through the detectors material elastic or inelastic collisions with shell electrons or the nucleus occur. An elastic collision is defined as the collision where no loss in total kinetic energy occurs, while in inelastic collisions part of the kinetic energy is transformed to other types of energy. The dominance of a certain process over the others depend on the particle energy and type.

The dominant mechanism used for radiation detection is ionization, that is inelastic collisions with electrons. The charged particle traversing the semiconductor detector material excites electrons from valence band to conduction band efficiently creating what is called electron-hole pairs. Under the influence of an electric field these free excited charge carriers can be transported towards the electrodes inducing a current which then can be measured. The amount of created e-h pairs is proportional to the absorbed energy. The energy loss probability distribution can be described by a Landau distribution.

The difference between energy gap and ionization energy is dispersed as phonons. The associated production of  $e$ - $h$  pairs and phonons results in a reduced statistical variance of the number of created  $e$ - $h$  pairs [28]. The reduction factor is called Fano factor which is material specific and results from the energy loss in a collision not being purely statistical. For example, if  $w$  is the average energy for a particle to produce a charge carrier in a detector, then the relative  $FWHM$  resolution for measuring the particle energy  $E$  is:  $R = 2.35\sqrt{\frac{Fw}{E}}$ .

### 3. PHYSICS OF SEMICONDUCTOR DETECTORS

---

The mean rate of energy loss by moderately relativistic charged heavy particles is well-described by the Bethe-Bloch equation [25]:

$$\left\langle -\frac{dE}{dx} \right\rangle = K z^2 \frac{Z}{A} \frac{1}{\beta^2} \left[ \frac{1}{2} \ln \left( \frac{2m_e c^2 \beta^2 \gamma^2 W_{max}}{I^2} \right) - \beta^2 - \frac{\delta(\beta\gamma)}{2} \right] \quad (3.1)$$

where

- $K = 4\pi N_A r_e^2 m_e c^2 = 0.30707 \text{ MeV/mol} \cdot \text{cm}$ ,
- $N_A = 6.02214 \times 10^{23} \text{ mol}^{-1}$ , Avogadro's number
- $r_e = e^2/4\pi\epsilon_0 m_e c^2 = 2.81794 \text{ fm}$ , the classical electron radius
- $m_e c^2 = 0.510998928 \text{ MeV}$ , the electron mass  $\times$  the speed of light squared ( $c = 299.792.458 \text{ m/s}$ )
- $\epsilon_0 = 8.85418 \times 10^{-12} \text{ F/m}$ , the vacuum permittivity
- $z$ , the charge number of the incident particle
- $\frac{Z}{A}$ , the ratio of the atomic number to the atomic mass ( $g/mol$ ) of the absorber
- $\beta, \gamma$  are the kinematic variables with their usual relativistic meanings
- $I \text{ (eV)}$ , the mean excitation energy

The energy loss depends quadratically on the charge of the traversing particle and the maximum energy transfer in a single collision for a particle with mass  $M$  is given by:

$$W_{max} = \frac{2m_e c^2 \beta^2 \gamma^2}{1 + 2\gamma m_e/M + (m_e/M)^2} \quad (3.2)$$

Moreover, the density correction ( $\delta(\beta\gamma)$ ) is introduced, having a significant effect towards relativistic energies as can be seen in Figure 3.1. As the energies increase, the electric field of a particle flattens and extends as  $\ln(\beta\gamma)$  but the medium it traverses becomes polarized and limits its extension. The density effect correction usually described by the Sternheimer's parametrization [10]. In the aforementioned figure we can also observe the energy region where *Bethe* equation is valid, that is for  $0.1 \lesssim \beta\gamma \lesssim 1000$ . With the proper inclusion of corrections [11] *Bethe* equation can be accurate to about 1% down to  $\beta \sim 0.05$  but for lower beta there is no satisfactory theory. Usually, the phenomenological fitting formulae from Andersen & Sieglar is used [12],[25].



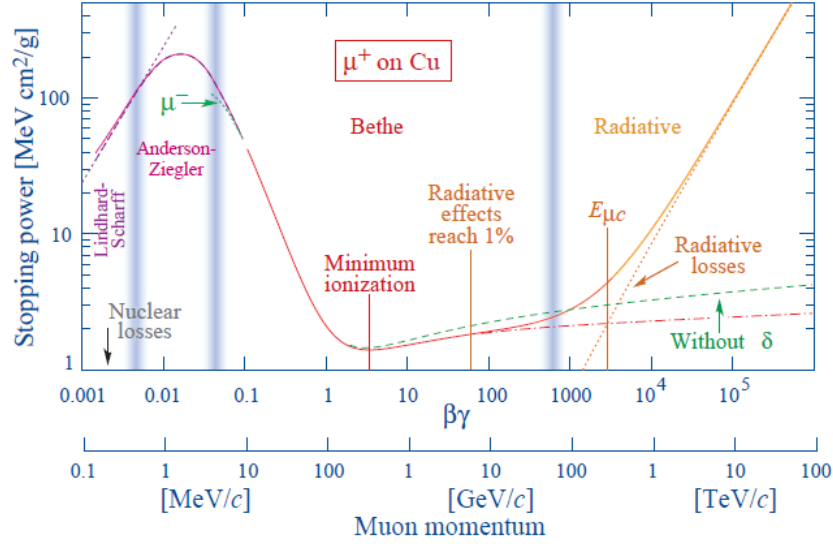


Figure 3.1: Stopping power of positive muons in copper as a function of  $\beta\gamma$  and momentum. The region described by Bethe is marked, and the effect of the density effect in high energies is also presented.

It should be noted that within the Bethe-Bloch equation the mean rate of energy loss is weighted by very rare events with large single-collision energy deposits. Most frequently the losses are small and especially in thin absorbers (like the detectors discussed in this work) the total energy loss will show a large variance. The energy loss probability distribution is adequately described by the Landau distribution. The Landau distribution (Figure 3.2) resembles a Gaussian distribution, only with a difference of a longer upper tail. This tail represents collisions which happen with a small probability mentioned above, each one of them transferring large amounts of energy [14]. The most probable energy loss in a detector is considerably lower than the mean given by the Bethe-Bloch.

The difference between the mean rate of energy loss and the most probable energy loss is depicted

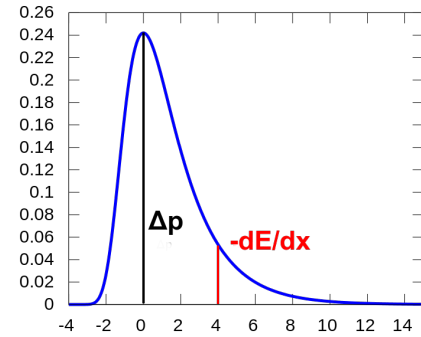


Figure 3.2: The PDF of Landau distribution with the most probable value ( $\Delta p$ ), and the mean rate of energy loss ( $-dE/dx$ ) quantitatively placed.

### 3. PHYSICS OF SEMICONDUCTOR DETECTORS

in Figure 3.3. We can observe that while  $-\langle dE/dx \rangle$  is independent of thickness,  $\Delta p/x$  is not. As a result, in silicon the most probable value would be approximately 70% and 65% of the mean loss for a detector of 300  $\mu\text{m}$  and 100  $\mu\text{m}$  respectively.

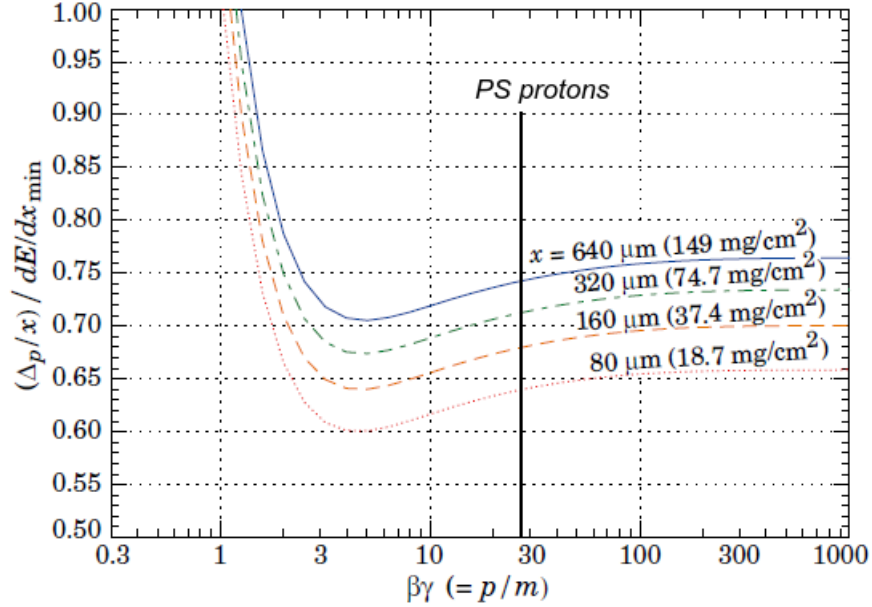


Figure 3.3: Most probable energy loss in silicon, scaled to the mean loss of a MIP [25].

#### 3.1.1 Minimum Ionizing Particles

Particles in the minimum ionization region  $\beta\gamma \gtrsim 3$  are called minimum ionizing particles (MIP). In practical cases, most relativistic particles have mean energy loss rates close to the minimum, meaning that they are MIPs. This situation occurs when the kinetic energy of the particle is at least twice larger than their rest mass. For example, protons can be considered as MIPs when their kinetic energy is greater than 2 GeV. For the sensors concerned in this work of thickness  $< 1$  mm the energy loss of a MIP is very small compared to the particle energy and homogeneously distributed along the detectors bulk. In Figure 3.4 the energy loss in relation to the absorber material atomic number is presented and the results for *Si* and *C* are also demonstrated in Table 3.1.

The energy deposition of a MIP can be calculated by:

$$E_{MIP} = -\left\langle \frac{dE}{dx} \right\rangle \rho d \quad (3.3)$$

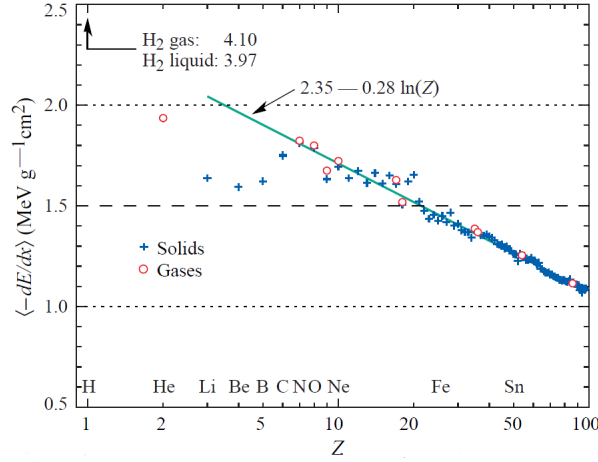


Figure 3.4: Stopping Power at minimum ionization for different chemical elements. For  $Z > 6$  a fit as of  $-\ln(Z)$  is depicted. A simple functional dependence on  $Z$  is not to be expected, since stopping power also depends on other variables [25]. Silicon and Carbon have an atomic number of  $Z = 14$  and  $Z = 6$  respectively.

where  $-\langle dE/dx \rangle$  the stopping power,  $\rho$  the target materials density and  $d$  the detector's thickness.

Finally, the charge created inside the detector would be:

$$Q_{MIP}(x) = \frac{1}{d} \frac{E_{MIP}}{E_{pair}} q_e \quad (3.4)$$

### 3.1.2 $\alpha$ -particles

Alpha particles consist of two protons and two neutrons bound together in a particle identical to a *Helium* nucleus. They are generally produced in the process of  $\alpha$  decay. Due to their production mechanism in standard radioactive decay,  $\alpha$  particles usually have kinetic energy of about 5 MeV and velocity of  $\beta = 0.05$ . During this work, a source of  $^{241}\text{Am}$  has been used for signal measurements as seen in the next chapter. The corresponding  $\alpha$  particles have energy of 5.637 MeV and  $\beta\gamma = 0.054$  for a mass of  $m_\alpha = 3.73 \text{ GeV}/c^2$ .

The energy deposition of  $\alpha$  particles at this low energy is not described by theory and so the use of experimental data was necessary. For that purpose, *SRIM* [32] software has been used to calculate the energy loss which is then inserted into the simulation discussed in the next chapter. More specifically, data for a helium ion hitting both

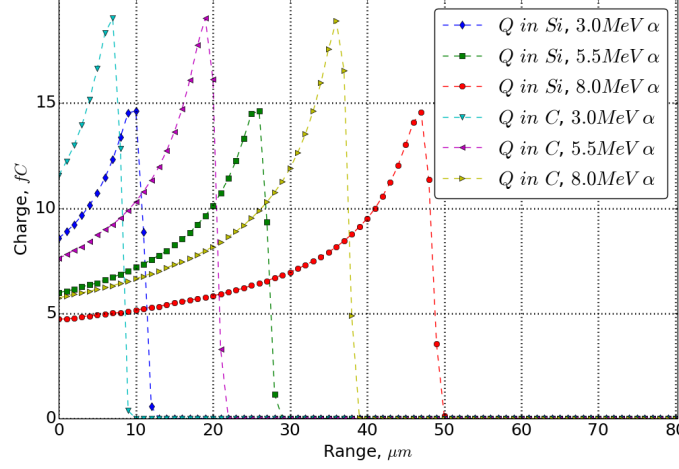


Figure 3.5:  $\alpha$ -particle range in *Si* & *C* and their respective Bragg curve displaying the energy deposition inside the target material.

silicon and carbon targets with different energies close to 5 MeV have been used for the simulation of  $\alpha$  – TCT on silicon and diamond detectors and can be seen in Figure 3.5. From the figure we can observe that an  $\alpha$ -particle loses most of its energy at the end of its trajectory, right before it comes into rest, forming the so called *Bragg Peak*. As a consequence, when  $\alpha$ -particles are stopped within the detectors material they deposit a large amount of energy locally creating areas with high charge carrier densities.

#### 3.1.3 Photons

Photons interacting with matter can be reflected, absorbed or transmitted through the material. When absorbed in a semiconductor, photons have the possibility to excite electrons providing enough energy to move them to the conduction band. The energy of the photon determines whether the photon will excite electrons or will simply be transmitted through the material. The energy (in eV) of a single photon depends on its wavelength as defined by:

$$E = \frac{hc}{\lambda} \quad (3.5)$$

where  $h = 6.626069 \times 10^{-34} \text{ J} \cdot \text{s}$  is Planck's constant,  $c$  the speed of light and  $\lambda$  the photons wavelength.

Throughout this work laser pulses in the range of 200 – 1100 nm are concerned. Ionization is possible to occur if the energy of the photon is higher than the detectors energy gap, which is true for wavelengths lower of 1127 nm for *Si* and lower of 225 nm for *sCVD* at room temperature. Instead of continuously losing energy, as in case of charge particle interaction, the number of photons (flux) is exponentially decreasing as:

$$\Phi(x) = \Phi_0 e^{-\sigma(\lambda)x} \quad (3.6)$$

where  $\Phi_0$  is the initial flux and  $\sigma$  the absorption coefficient.

The absorption coefficient depends on the wavelength of the pulse and is experimentally defined for each material.

The specification of the laser source provides the information for the energy and spatial distribution of the pulse, thus affecting the created charge distribution inside the detectors bulk.

A simplified model results in the total charge expected based on the energy of the lasers pulse, and the given exponential decrease of the number of electrons.

$$Q_{l_{tot}} = \int_0^d q_0 e^{-\sigma x} \Rightarrow q_0 = \sigma Q_{l_{tot}} \quad (3.7)$$

and finally similarly to Equation 3.6:

$$Q_l(x) = q_0 e^{-\sigma(\lambda)x} \quad (3.8)$$

where  $Q_{l_{tot}}$  is the total charge created,  $q_0$  is the initial charge at the surface of the detector, and  $\sigma$  the absorption coefficient.

An example of the above mentioned model is presented in Figure 3.6 where the absorption difference for different wavelengths in silicon is shown. The 670 nm laser attenuates fast, creating *e-h* pairs only at the surface of the detector, making it ideal for TCT measurements. On the other hand, the 1060 nm laser distributes charge equally along the detectors bulk similarly to a MIP.

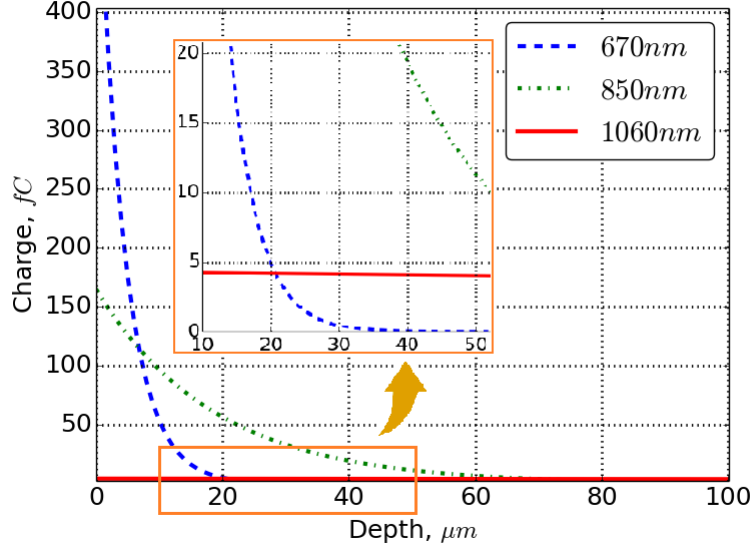


Figure 3.6: Charge creation from laser source of different wavelengths inside the bulk of a *Si* detector.

## 3.2 Semiconductor Detectors

Semiconductor detectors are widely used in a variety of applications due to their unique combination of energy and position resolution. They are essentially a solid-state ionization chamber, but the main advantages of having a solid medium compared to the chambers gas medium are the lower energy needed to create  $e-h$  pairs and the greater density. More specifically, the energy to create  $e-h$  pairs, which is proportional to the energy gap ( $E_{\text{pair}} \propto E_g$ ), is  $\sim 10$  times smaller than for gas ionization, providing increased charge (better energy resolution) and the higher density means that the range of secondary electrons is reduced resulting in excellent spatial resolution. Smaller  $E_g$  would produce higher signal but the intrinsic resistance of the material is also critical. As the band gaps decrease, thermal excitation (given by Fermi-Dirac Distribution Equation 3.9) will promote electrons into the conduction band and increase their concentration exponentially.

$$f(E) = \frac{1}{1 + e^{(E-E_F)/kT}} \quad (3.9)$$

The detector materials concerned in this work are silicon and diamond. The basic properties of these materials are summarized in Table 3.1.

### 3.2. SEMICONDUCTOR DETECTORS

Quantity ,	$[representation], [units]$	<i>Si</i>	<i>sCVD</i>
Band Gap (RT),	$[E_{gap}], [eV]$	1.12	5.48
Band Gap (LHe),	$[E_{gap}], [eV]$	1.17	5.45
Fano Factor,	$[F], [\#]$	0.115	0.08
Energy needed for the creation of one $e-h$ pair, $[E_{pair}], [eV]$		3.6	13
Ionization Loss from MIP, $[-\langle dE/dx \rangle / \rho], [MeV cm^2/g]$		1.67	1.76
Mean created charge per $100\mu m$ ,	$[Q(0)/100\mu m], [fC]$	1.73099	0.762438
Most Probable charge per $100\mu m$ ,	$[Pairs/100\mu m], [\#]$	7500	3600
Displacement Energy,	$[E_d], [eV]$	25	43
Breakdown Field,	$[V_{br}], [V/\mu m]$	30	1000

Table 3.1: Basic properties of Silicon and Diamond detector materials.

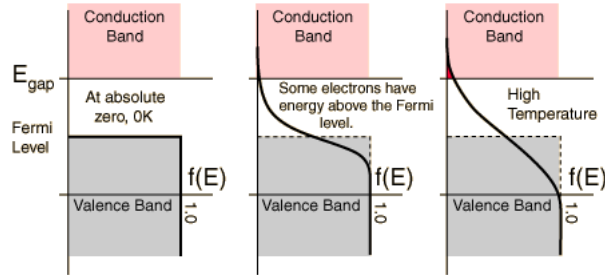


Figure 3.7: At high temperatures or with a low  $E_g$  electrons can reach the conduction band.

#### 3.2.1 Depletion Region

As previously shown in Table 3.1, a MIP crossing a  $300\text{ }\mu\text{m}$  detector could create up to  $\approx 22.400$   $e$ - $h$  pairs. However, thermal excitation creates free carriers in both bands which -when the material has not had impurities added to it- is called intrinsic carrier concentration. This concentration depends on the energy gap of the material and on its temperature and for silicon is modelled as in Equation 3.10 [15] for temperatures in the range of  $78 - 340$  K. Consequently, given a silicon detector of  $300\mu\text{m}$  thickness and area of  $36\text{ mm}^2$  the existing free carriers in the detectors bulk are  $n_i \cdot A \cdot d \approx 10^8$  at room temperature. At lower temperatures, or in materials with higher energy gap (like diamond) thermal excitation is of minor significance.

$$n_i(T) = 5.29 \times 10^{19} (T/300)^{2.54} e^{(-6726/T)} \quad (3.10)$$

Therefore, free carriers must first be removed in order to create a depleted area, where charge generation is only due to radiation particles. It is typically accomplished using reversely-biased p-n junction. The width of the depletion region can be calculated solving the Poisson equation using the conservation of charge  $N_A d_p = N_D d_n$  resulting in:

$$W = \sqrt{2\epsilon(V + V_{bi})/|N_{eff}|e} = \sqrt{2\rho\mu\epsilon(V + V_{bi})} \quad (3.11)$$

where  $V$  the external bias voltage,  $V_{bi}$  the built-in voltage,  $N_{eff}$  the effective doping concentration,  $e$  the electronic charge,  $\epsilon$  the dielectric constant,  $\rho$  the resistivity and  $\mu$  the charge carrier mobility.

A detector is fully depleted when the width of the depletion region is equal or higher to its thickness. Alternatively, by setting the detectors thickness as the depletion ( $W = d$ ) width and neglecting the built-in voltage which is usually very small, one can calculate the voltage needed for full depletion to be achieved as:

$$V_{fd} = \frac{e|N_{eff}|d^2}{2\epsilon} = \frac{d^2}{2\epsilon\mu\rho} \quad (3.12)$$

#### 3.2.2 Drift Velocity of carriers

The absorbed ionizing radiation creates  $e$ - $h$  pairs which, under the influence of an electric field move towards their respective electrode. This motion induces a current in an external circuit which then can be amplified and sensed. The shape of the signal depends on the carrier velocity and the electrode geometry, generally being a function of time evolution of carriers distributions. The charge collection time is the time needed by the charge carriers to reach their respective electrode, and is inversely proportional



to the average *drift velocity* of the carriers.

$$v_{drift} = \frac{d}{t_{drift}} \quad (3.13)$$

The drift velocity is linearly dependent on the existing electric field. By also introducing low-field mobility and saturation velocity, the transient drift velocity can be also described as [16]:

$$v_{drift_{e,h}} = \frac{\mu_{e,h}E}{1 + \frac{\mu_{e,h}E}{v_{sat}}} \quad (3.14)$$

where  $\mu$  the mobility of the carrier,  $E$  the existing electric field and  $v_{sat}$  the saturation velocity of the carrier.

From the Equation 3.14 we can deduce that the drift velocity can be further increased - and thus the charge collection time reduced - by increasing the applied bias voltage, until the saturation velocity is reached. Consequently, as most semiconductor detectors are thin ( $d < 1$  mm), the produced signals are fast of the order of nano seconds.

### 3.2.3 Weighting & Electric Field

The electric field is a critical parameter for the movement of the carriers inside the detector's bulk and thus the shape of the signal. When a detector is partially depleted the electric field is similar to that for a uniform space charge in the depleted region falling to near zero at the edge of the depleted region (Figure 3.8), while when operated with "overbias", that is the bias voltage exceeding the depletion voltage, a uniform electric field is formed.

The electric field is obtained through Poisson equation (Equation 3.15) after solving with  $\vec{E} = -\nabla V$  while the *Laplace* equation (Equation 3.16) provides the corresponding weighting potential and field.

$$\nabla^2 V = \frac{q_0 N_{eff}}{\epsilon \epsilon_0} \quad (3.15)$$

$$\nabla^2 V_w = 0 \quad (3.16)$$

The weighting potential describes the coupling of a charge at any position to a specific electrode. It is obtained by setting the potential of the specific electrode to 1 and all others to zero. The weighting field is defined similarly; all charges are removed and the measurement electrode raised to unit potential while all other electrodes are grounded.

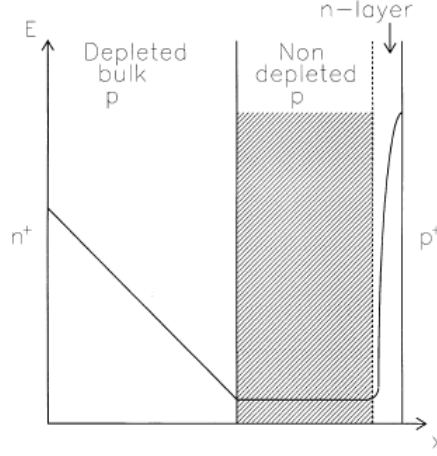


Figure 3.8: A schematic diagram of the electric field pattern inside a partially depleted irradiated silicon detector. The width of the high electric field region adjacent to the  $p^+$  side may be quite small [17].

It should be noted that electric and weighting field are distinctly different as the first determines the charge trajectory and velocity while the latter depends on the geometry and determines how charge motion couples to a specific electrode. In two-electrode configurations - as the ones concerned in this work - the electric and weighting field have the same form [24].

#### 3.2.4 Charge carrier mobility

Mobility is a quantity expressing how quickly a charge carrier can move through a semiconductor (or metal) when pulled by an electric field. Carrier mobility is different between materials and also depends on the materials temperature.

In silicon the mobility is sufficiently described in function of temperature by the Equation 3.17, 3.18 down to 50 K. Towards cryogenic temperatures mobility saturates at  $(8.27 \pm 0.66 \times 10^4) \text{ cm}^2/\text{Vs}$  for electrons and  $(2.37 \pm 0.6 \times 10^4) \text{ cm}^2/\text{Vs}$  for holes [5].

$$\mu_e(T) = 9.97534 \times 10^7 \cdot T^{-2.1330695} \cdot e^{(1-T/308777990)} \quad (3.17)$$

$$\mu_h(T) = 854 \times 10^3 \cdot T^{-1.075} \cdot e^{(1-T/124)} \quad (3.18)$$

For the modelling of the carriers mobility in diamond material a combination of two

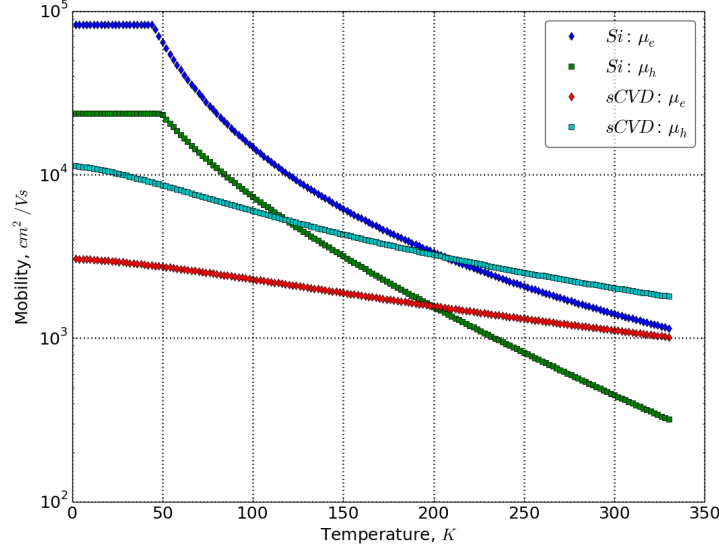


Figure 3.9: Temperature dependence of the carrier mobility in Si and CVD.

sources of scattering was considered. For temperatures between 200 – 300 K the low-field mobility is limited by the *acoustic phonon scattering (APS)* following a behaviour like  $\mu_{APS} \propto T^\alpha$ ,  $\alpha = -1.5$  described through the fit  $\mu_{APS}(T) = \mu_0(\frac{T}{300})^\alpha$ . For lower temperatures a saturation is observed due to the *neutral impurity scattering (NIS)*, that is the scattering of free charge carriers off neutral impurities which is independent of temperature. Following the *Matthiessen's rule* for the combination of  $\mu_{APS}$  &  $\mu_{NIS}$  results in [29]:

$$\mu_{NIS+APS}(T) = \left( \frac{1}{\mu_{NIS}} + \frac{1}{\mu_{APS}(T)} \right)^{-1} \quad (3.19)$$

Based on work & data presented in [29], the temperature independent factors are experimentally defined as  $\mu_{NIS}^h = (11300 \pm 120) \text{ cm}^2/\text{Vs}$  and  $\mu_{NIS}^e = (3058 \pm 27) \text{ cm}^2/\text{Vs}$ , while for the APS in the region 200 – 300 K,  $\mu_0$  is  $1.757 \times 10^3 \text{ cm}^2/\text{Vs}$  and  $2.471 \times 10^3 \text{ cm}^2/\text{Vs}$  for electrons and holes respectively.

### 3.2.5 Saturation Velocity

In all semiconductors there is a state (called *state of velocity saturation* where increasing electric field will not result to higher drift velocity. That means that for given charge carrier concentration and temperature there is a maximum possible current. This hap-

### 3. PHYSICS OF SEMICONDUCTOR DETECTORS

---

pens due to the fact that in their movement the charged carriers lose energy through increased levels of interaction with the lattice, by emitting phonons and even photons provided that the energy is large enough.

For the modelling of the saturation velocity dependence to temperature in silicon material a parametrization is shown in Equations 3.20 and 3.21 for electrons and holes respectively [19].

$$v_{sat_e} = 15857000 \times e^{-0.0013816 \cdot T} \quad (3.20)$$

$$v_{sat_h} = 14445000 \times e^{-0.0022938 \cdot T} \quad (3.21)$$

For diamond, a simple model which is common for electrons and holes as in Equation 3.22 is provided in [18].

$$v_{sat} = \sqrt{\frac{8E_{opt}}{3\pi m_{dos}} \tanh\left(\frac{E_{opt}}{2k_B T}\right)} \quad (3.22)$$

where  $E_{opt} = 163$  meV is the optical phonon energy, the energy that when the carriers surpasses their velocity saturates,  $m_{dos} \approx 0.5$  and  $k_B$  the Boltzmann constant.

However, it should be noted that there is a significant variance in measured saturation velocities and considerable uncertainty concerning the density of states effective mass [29],[19].

#### 3.2.6 Shockley-Ramo theorem

The *Shockley-Ramo* theorem provides an easy way of calculating the instantaneous current induced by moving charges in the vicinity of an electrode. It is based on the concept that current induced in the electrode is due to the instantaneous change of electrostatic flux lines which end on the electron, not the amount of charge received by electrode per second. The theorem states that the charge  $Q$  and current  $i$  induced by a moving point charge  $q$  are given by [20],[21],[22]:

$$Q = -q\Phi_w(x) \quad (3.23)$$

$$i = E_w(x) \cdot q \cdot v \quad (3.24)$$

where  $v$  is the instantaneous velocity of the point charge  $q$  while  $\Phi_w$  and  $E_w$  are the weighting electric potential and weighting electric field respectively.

As previously mentioned, the  $\Phi_w$  and  $E_w$  are the potential and electric field that would exist if all charges are removed, the selected electrode set at unit potential and all other electrodes set at zero potential. It is valid when charge is conserved in the transport step between two subsequent instances. It is therefore obvious that the weighting potential and field depend on the configuration of the electrodes.

In the case of pad diodes, mostly concerned in this work, the weighting potential is given by the induced charge on one of the planes of an infinite parallel plate capacitor as function of the distance to it. It is linear and provided that the sensor is fully depleted, can be calculated as [28]:

$$\Phi_w(x) = 1 - x/d \quad (3.25)$$

### 3.3 Radiation Damage

Radiation damage in semiconductor devices can be roughly divided in two mechanisms: surface and bulk damage. Surface damage affects mainly segmented detectors (strips, pixels). The positive charge gets accumulated (trapped) near the insulating  $\text{SiO}_2$  elements, thus affecting the shape of the bias field and leading to various failures like breakdown voltage.

Bulk damage on the other hand, refers primarily to the interaction of high energy particles with the crystal structure of the detectors. The primary damage mechanism is the displacement of a *primary knock on atom* (PKA) out of its lattice site, resulting in point defects, that is an interstitial and a left over vacancy (Frenkel pair). Moreover, it is possible that along its path, this recoil atom also loses its energy through ionizing and non-ionizing contributions. While the former will not result in any change to the crystal structure of the device, the latter are prevailing especially towards the end of the recoil atoms path. There, dense agglomerations of defects are formed referred to as defect clusters. The displacement energy, that is the energy needed for a primary recoil atom to be displaced, for *Si* and *sCVD* can be seen in Table 3.1. A higher displacement energy threshold could be interpreted as a more radiation hard material.

Radiation damage produced by different types and energies of particles can be scaled and appropriately described by the *Non-Ionizing Energy Loss* (NIEL) hypotheses. The basic assumption of NIEL is that any damage in the materials lattice scales linearly to the energy transmitted in displacement collisions, without taking into account spatial parameters or annealing processes. The NIEL hypotheses leads to the determination of hardness factors, enabling the comparison and calculation of the radiation damage of different sources [26], [23].

#### 3.3.1 Effects of radiation damage on detectors

There is a significant active research on the classification and definition of the electrical properties of each type of occurring defect. These microscopic defects relate to changes in the detectors properties from a macroscopic perspective. These changes can decrease the SNR or even lead to the failure of a sensor. The main detector properties affected by radiation damage are:

- Leakage current
- Depletion Voltage
- Charge Collection Efficiency (CCE)

##### Leakage Current

Leakage current can be divided in *diffusion* current and *generation* current. The first refers to charges generated in the non-depleted zone diffusing into the depletion region and is the only component of the leakage current in an ideal diode. It is very sensitive to manufacturing processes, so quality control and the use of pure and defect free material is crucial for its amplitude. The second can be further divided in *bulk* or *surface* generation current. Bulk generation current occurs due to thermal generation or due to  $e-h$  pair generation at radiation induced defects which are energetically located close to the middle of the band gap while the latter is due to radiation induced  $\text{SiO}_2 - \text{Si}$  states. Depending on the kind of radiation and the structure of the diode the one or the other component dominates [27],[23].

Radiation induced defects close to the middle of the band gap are generating  $e-h$  pairs thus increasing the leakage current. This increase leads to inaccurate measurements & decrease of the SNR. Leakage current scales linearly to the absorbed dose and can be described as  $\Delta I_1 = \alpha \Phi$  per unit volume with  $\alpha$  describing the damage coefficient ( $\approx 3 \cdot 10^{17}$  A/cm) and  $\Phi$  the absorbed dose. Additionally, generation current strongly depends on the temperature as follows:

$$\frac{I_R(T_2)}{I_R(T_1)} = \left(\frac{T_2}{T_1}\right)^2 \exp\left(-\frac{E_g}{2k} \frac{T_1 - T_2}{T_1 T_2}\right) \quad (3.26)$$

where  $E_g$  denotes the band gap and  $T_1$  &  $T_2$  the temperatures in question [26]. It is therefore evident that cooling can significantly reduce the leakage current.

### Depletion Voltage

Depletion voltage (also discussed in section 3.2.1) signifies the bias required for the junction to be fully depleted. As it can be deduced from Equation 3.12 defects contributing to the space charge density  $N_{\text{eff}}$  also have an effect on depletion voltage as  $V_{\text{depl}} \propto |N_{\text{eff}}|$ . The effective doping concentration is often parametrized through the *Hamburg* model as a function of fluence and annealing time as seen in Equation 3.27

$$\Delta N_{\text{eff}}(\Phi_{eq}, t(T_\alpha)) = N_A(\Phi_{eq}, t(T_\alpha)) + N_C(\Phi_{eq}, t(T_\alpha)) + N_Y(\Phi_{eq}, t(T_\alpha)) \quad (3.27)$$

where the three components  $N_A$ ,  $N_C$  and  $N_Y$  describe the short term annealing, the stable component and the long term reverse annealing respectively. For more information the reader is encouraged to follow the provided literature [23], [27].

As a result, an increase in depletion voltage would result in increased noise and would require the detector to be biased higher increasing the power consumption and eventually being limited by the breakdown voltage of the detectors material (Table 3.1).

### Charge Trapping

Trapping refers to the capture of drifting charges by deep defects of different energy levels in the crystal lattice of the semiconductor. If the trapping duration is longer than the time needed for the pulse to be shaped by the read-out electronics trapping results in reduced CCE, lower signal and consequently lower SNR. The trapping probability of electrons or holes depends on the capture coefficient of the type of the specific defect, its concentration and the fraction not occupied with electrons [23]. Inverse processes also can happen, that is after a certain time the trapped charge gets thermally excited and de-trapped.

The charge carriers trapping time constant is:

$$\tau_t = \frac{1}{\sigma_{e,h} v_{th}(T) N_t} \quad (3.28)$$

where  $\sigma_{e,h}$  is the trapping cross section for each carrier,  $v_{th} \approx \sqrt{\frac{3k_B T}{m^*}}$  the thermal velocity and  $T$  the absolute temperature and  $N_t$  is the traps density of the deep level.

The de-trapping constant depends exponentially to the lattices temperature as described by:

$$\tau_d = \frac{e^{E_a/k_B T}}{\sigma v_{th}(T) N_t} \quad (3.29)$$

### 3. PHYSICS OF SEMICONDUCTOR DETECTORS

---

where  $E_a$  is the activation energy, and  $k_B$  the Boltzmann constant.

De-trapping times are of the order of  $ps$  or  $ns$  at RT and increase in LHe temperature to the order of  $\mu s$  or even days [5], [29]. In general, trapped carriers in LHe temperatures are removed from the contribution to the pulse formation.

The number of defects in the detectors material is proportional to the radiation dose accepted  $N_{def}(\phi) \propto \phi$ . On the other hand, charge carriers lifetime is inversely proportional to the number of defects and thus to the accepted fluence as well  $\frac{1}{\tau_i(\phi)} \propto N_{def}(\phi)$ . Hence:

$$\tau_i(\phi) = \left( \frac{1}{\tau_i(0)} + \phi^s k \right)^{-1} \quad (3.30)$$

where  $k = \frac{d \frac{1}{\tau_i(\phi)}}{d\phi}$  is the damage constant and  $\tau_i(0)$  is a constant describing the initial lifetime in conditions of zero radiation dose accepted. The  $s$  parameter was introduced in [5] clearly improving the fit, but its physical origin and explanation is yet unclear.

Based on the above charge lifetime and the Hecht equation a charge degradation model has been presented in [5]. The model considers MIP sources creating charges throughout the detectors thickness and takes into account both electrons and holes and is presented in the following equation:

$$Q_{MIP}(\phi) = Q_{MIP}(0) \sum_{i=e,h} \frac{\mu_i E \tau_i(\phi)}{d} \left[ 1 - \left( \frac{\mu_i E \tau_i(\phi)}{d} \right) (1 - e^{-\frac{d}{\mu_i E \tau_i(\phi)}}) \right] \quad (3.31)$$

where  $\mu$  the mobility of each carrier,  $E$  the electric field and  $d$  the detectors thickness.

Therefore, The CCE can be at once defined as the ratio between the collected charge, to the initially created charge.

$$CCE = \frac{Q_c}{Q_0} \quad (3.32)$$

Based on the above equations, one can also define the distance a carrier travels throughout its lifetime before being trapped, that is the *mean free path* (MFP). The MFP is a function of the charge lifetime, the carriers mobility and the existing electric field  $\lambda = \mu E \tau_i$ . As  $\lambda \propto \tau_i$  one could also express the MFP as a function of the fluence according to Equation 3.30 as below:

$$\lambda(\phi) = \left( \frac{1}{\lambda(0)} + \phi k' \right)^{-1} \quad (3.33)$$



Similarly, the CCD is defined as:

$$CCD = \frac{Q_c}{Q_0} d \quad (3.34)$$

Note that while the MFP can be larger than the detectors thickness, this is not possible for the CCD [5].

# The Transient Current Technique & Simulation

## 4.1 The Transient Current Technique

The Transient Current Technique is a well established current measurement method for semiconductor detector characterization and it is the most widespread method for analysing pad diode detectors. It has been applied to both insulators and semiconductors. TCT is usually used in a metal-semiconductor-metal structure, where the semiconductor is used as a solid-state ionization chamber.

Using highly ionized  $\alpha$  particles ,*e.g.*  $^{241}\text{Am}$  (Figure 4.1), or a laser of appropriate wavelength ,*e.g.* red laser for *Si*, local, free charge is deposited close to the electrode. Laser sources provide better SNR due to the ability of direct oscilloscope triggering by the excitation pulse and the exact focusing of the optical beam onto a specific detector spot. The illumination is usually done from the heavily doped extremes of the detector. Since charge is released only in the first few  $\mu\text{m}$  of the device, the observable current is only related to the contribution of just one type of charge carrier, depending on the polarization or the illuminated side of the detector 4.2.

These charge carriers drift under the influence of an electric field that exists inside the reverse biased diode. Their drift induces a time-resolved current which can be amplified and read from external electronics with a high bandwidth.

TCT utilizes this drift and provides a direct way to measure the transit time, that is the time needed for the carriers to reach their respective electrode. The extracted current pulse contains information about the amount of drifting charge and its drifting velocity. As the charge drift is influenced by the detector material properties, useful information can be derived from the shape of the current pulse.

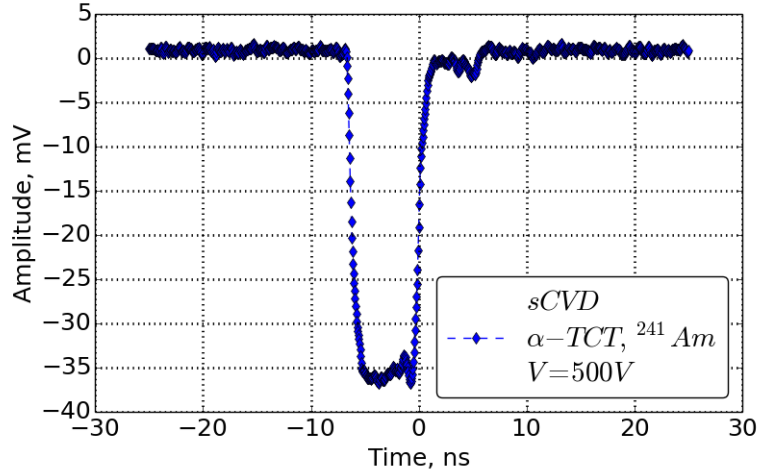


Figure 4.1:  $\alpha$ -TCT with  $^{241}\text{Am}$  on a sCVD sample acquired from a 2.5GHz oscilloscope. This test was not performed in vacuum, so energy loss due to the 3 mm air layer between source and detector should be taken into account.

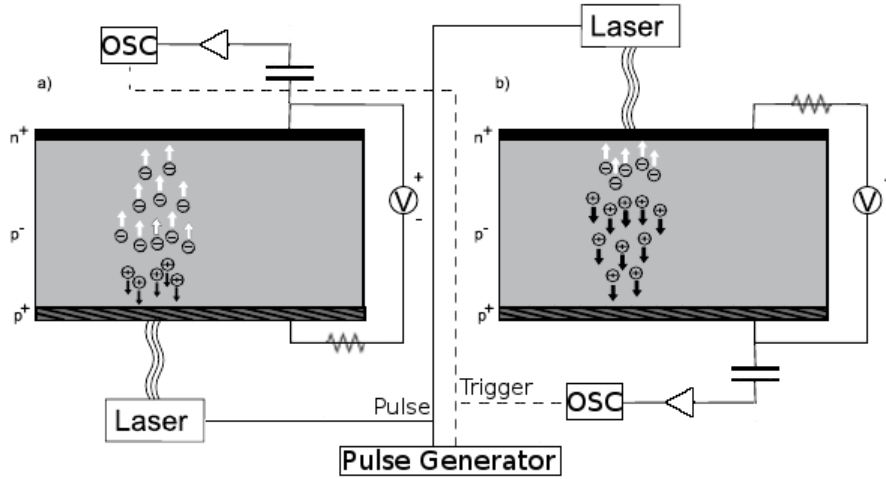


Figure 4.2: A typical TCT setup. Illumination of the detector from different sides with a laser source induces current mostly contributed from one type of charge carrier. Modified from [30].

TCT analysis provides information on:

- Electric field distribution
- Full depletion voltage
- Charge trapping & de-trapping (effective trapping time)
- Charge Collection Efficiency
- Sign of the space charge
- Charge Carrier drift velocities & mobilities

As TCT focuses at the transient phenomena occurring inside the detector's bulk, limitations arise when surface effects are becoming dominant mainly for MIPs and  $\alpha$ -particles. Also, uncertainties exist for laser TCT as the laser light transmission from the laser head to the detector surface is expected to be temperature dependent [5].

Finally, different types of the TCT have been developed, each focusing in their respective area of interest. As a result, techniques such as *e-TCT* (edge-TCT), *c-TCT* (cryogenic-TCT), *TPA-TCT* (Two Photon Absorption-TCT ) have been developed, demonstrating the importance of TCT in detectors characterization.

### 4.2 TCT Simulation Application

As part of the study of transient phenomena in semiconductors, a simulation application was developed. This application provides the ability of a fast simulation of the charge creation and drift inside the detectors bulk. The detector materials under investigation are silicon and diamond. Furthermore, different types of excitation are taken under consideration such as low energy  $\alpha$ -particle, MIP and laser sources.

Looping over the detectors depth and time provides the necessary information about the charge carriers movement and consequently the induced current. The attempted simulation is only for one dimension, thus edge effects on large pad detectors such as CryoBLMs can be neglected. This final goal of the project is to provide a definition of the weighting and electric field inside the detectors bulk, generate the charge deposition based on the selected source and finally extract the detector's signal response based on the Shockley-Ramo's theorem 3.24.

In the following, a detailed description of the simulation algorithm and the applications structure is presented.

### 4.2.1 Pulse Shaping Algorithm

The simulation's first step is to provide all the detector material properties based on the given temperature. The temperature dependent properties for silicon and diamond material covered in this simulation are the energy gap ( $E_g$ ), the charge carrier mobilities ( $\mu_{e,h}$ ) and saturation velocities ( $v_{sat_{e,h}}$ ). Their parametrization has been described in the previous chapter. Still, the user is also able to manually change the input values.

The next step is to define the fields inside the detectors bulk. Therefore, a solution of the Poisson's 3.15 and Laplace's 3.16 equations is attempted for the definition of the electric and weighting field distribution respectively. The Dirichlet boundary conditions are the known potential in each side of the detector, which are defined as input parameters,  $V_{in}$  &  $V_{out}$ .

In the case of pad diodes where only two electrodes are present, the solution is linear and given by Equation 3.25, provided that the detector is fully depleted. As the purpose of this simulation is also to investigate damage phenomena in detectors, cases such as non fully depleted detectors or traps causing centres of different electric properties should also be taken under consideration. Hence, a numerical solution based on the *Jacobi* iterative method to the above equations is also provided.

For the numerical solution the discrete form of the Poisson's equation must be used 4.1. To discretize Poisson's equation, the spatial derivatives of the potentials need to be approximated. Considering one dimensional space, the Taylor series expansion of the two neighboring components is presented in 4.3, 4.2 and by adding them together we conclude to the Jacobi's iterative procedure solution 4.4. Similar solution can be applied for the two-dimensional space, and it is described widely in literature [31].

$$\frac{d^2}{dx^2}V(x) = -f(x) \quad (4.1)$$

$$V(x+h) = V(x) + \frac{h}{1} \frac{d}{dx}V(x) + \frac{h^2}{2} \frac{d^2}{dx^2}V(x) + \frac{h^3}{3} \frac{d^3}{dx^3}V(x) + \dots \quad (4.2)$$

$$V(x-h) = V(x) - \frac{h}{1} \frac{d}{dx}V(x) + \frac{h^2}{2} \frac{d^2}{dx^2}V(x) - \frac{h^3}{3} \frac{d^3}{dx^3}V(x) + \dots \quad (4.3)$$

$$V^{n+1}(x) = \frac{1}{2}(V^n(x+1) + V^n(x-1) + h^2 f(x)) \quad (4.4)$$

Subsequently, a charge distribution is introduced based on the parameters selected. The user has at his disposal options for  $\alpha$ -particle, laser sources and MIP. The energies available for the  $\alpha$ -particles range from 3 MeV to 8 MeV and their deposited charge depth dependence is simulated using *SRIM* program [32]. The laser sources are parametrized based on their power and pulse duration so that the total energy of the pulse can be

derived. The wavelength input will determine the absorption coefficients in each material, which are extracted from [33], [34] and inserted to the simulation. Then the charge distribution is calculated as described in Section 3.1.3. In the case of MIPs, the only parameter provided is the rate of energy loss and the created charge is homogeneously distributed as presented in section 3.1.1. Finally, for further potential and flexibility, the user has the ability to introduce a file describing an arbitrary charge distribution.

Having defined the field distribution and the charge deposition, the application proceeds in simulating the transient phenomena. The detector thickness is divided in bins with a predefined width of ( $1\mu m$ ). Moreover, the time steps taken by the simulation are parametrized from the user. The existing electric field in each position (bin) of the detector causes the charges to accelerate to a specific speed,  $v \rightarrow f(x, T)$ . The acceleration of the charges is considered instantaneous and is not taken into account. The speed of the charges in each bin is now discretized as:

$$v_{drift_{e,h}}(x, T) = \frac{\mu_{e,h}(T)E(x)}{1 + \frac{\mu_{e,h}(T)E(x)}{v_{sat_{e,h}}(T)}} \quad (4.5)$$

The output current is then calculated based on 3.24 as:

$$I(t) = \sum_0^d i(x) = \sum_0^d q(x)v(x, T)E_w(x) \quad (4.6)$$

The current version of the application (*v2.2*) includes the option of simulating the affects of radiation damage in the form of trapping. More precisely, based on the input of the accepted dose provided by the user, the algorithm determines the charge lifetime (Equation 3.30) and therefore removes the remaining drifting charge carriers at the calculated moment.

Finally, the front-end electronics, that is the amplifier and the oscilloscope, were described with a simple approach. Based on their characteristics such as the input impedance and bandwidth for oscilloscope and additionally the gain for the amplifier an appropriate RC shaping of the pulse was produced.

The above procedure is depicted in a graph form in the Figure 4.3. In addition, the GUI developed to serve this functionality is presented in Figure 4.4. More details on the structure of the software are provided in the next section.

### 4.2.2 Software Description

Taking under consideration that the subject of the simulation is within a very active area of research, where detector modelling is constantly progressing, the structure of this project was attempted to be very modular and facilitate further expansion.

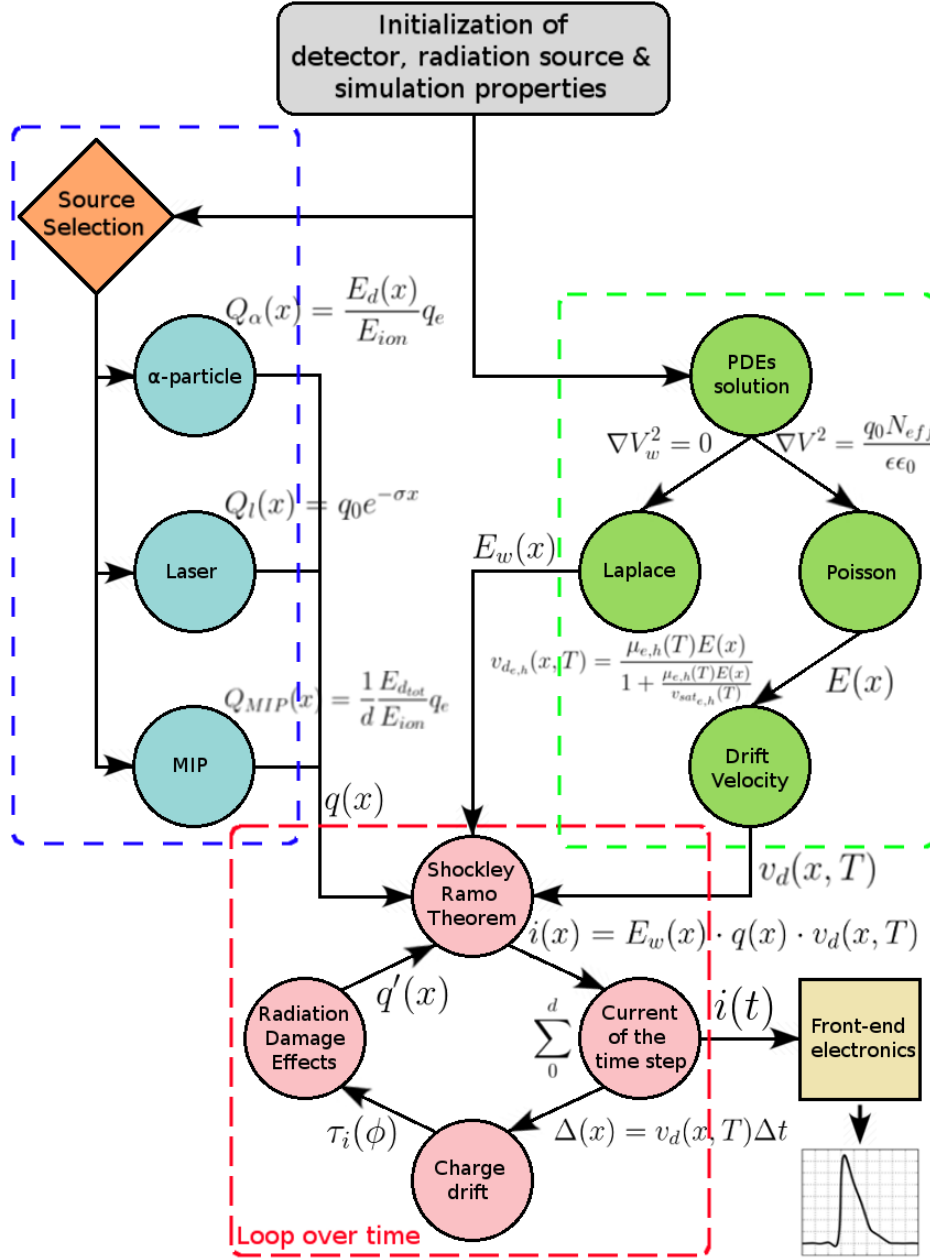


Figure 4.3: A block diagram of the algorithm implemented for the signal formation.

## 4. THE TRANSIENT CURRENT TECHNIQUE & SIMULATION

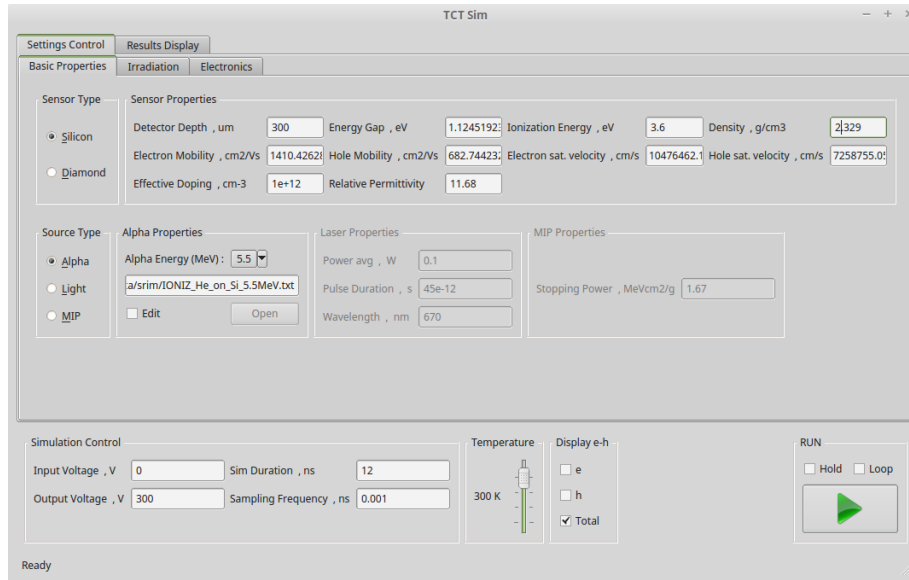


Figure 4.4: The main window of the TCTsim application. From the first tab, the user can select and alter options related to the detector material properties, the radiation source type as well as simulation factors such as bias, temperature or sample frequency.

The application was developed using the programming language Python and the PyQt graphical framework. Additionally, for the performed calculations and the resulting plots there have been extensive use of the Numpy and Matplotlib core packages of the Scipy open-source software ecosystem (Fig.4.5).



Figure 4.5: Python along with PyQt, Numpy and Matplotlib were used for the development of the TCTsim application.

The starting **GUI class**, sets the initial structure of the application. As can be seen in Fig.4.4 the GUI is divided in a lower and an upper part. The former contains all the general simulation controls, while the latter contains two rows of tabs, each one serving a purpose explained later.



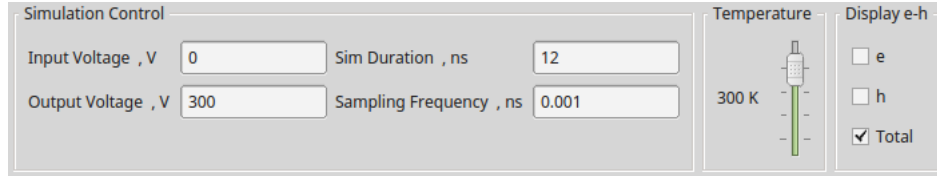


Figure 4.7: The SimControl widget contains the data and options of the displayed parameters.

All the building blocks of the application have been designed as separate **QWidget** **classes** being -in most cases- the interface of other computation classes.

The **SimControl** class mentioned earlier (Fig.4.7), sets the GUI of the lower part of the application, but it also serves as data storage for variables such as  $V_{input}$  &  $V_{output}$ , the *sim duration* & the *sampling frequency* which are displayed as text fields. Also, a slider controlling the *temperature* triggers the recalculation of all the temperature dependent detector properties through the **Sensor** class in real-time. Moreover, options concerning the final display of electrons and holes contribution to the current pulse are provided as check-boxes. Last, the *Run box* (Fig.4.6) contains the button which starts the algorithm and the options "*Hold*" and "*Loop*" which refer to the potential of keeping the previously calculated data for comparison reasons, as well as iterating over different simulation settings respectively.



Figure 4.6: The "Run box" is part of the SimControl widget.

The **Sensor** class consists of the interface between the user and the sensor modelling (Fig.4.8). Initially, it consists of a static list of radio buttons (Sensor Type), each one activating a specific class containing the properties and the modelling of each detector type. Currently, the **Silicon** class and the **Diamond** class represent each detector material according to the models presented in *chapter 3*. Each of those class contain two public instance variables (namely *labels* and *data*) which are collected from the **Sensor** class and appropriately displayed to the user. In the case that the user will select a different detector, the previous object is destroyed and the new one takes over the same role. This design offers great flexibility in the case that additional detector modelling is desired to be introduced. Any new class satisfying the public interface for the **Sensor** class can implement a new modelling and be added to the simulation.

The design approach mentioned above has also been followed in the **Source** class and the **Electronics** class with only a few differences.

The **Source** class (Fig.4.9) again creates a static widget displaying the options

#### 4. THE TRANSIENT CURRENT TECHNIQUE & SIMULATION

Sensor Type		Sensor Properties						
<input type="radio"/> Silicon	Detector Depth , um	500	Energy Gap , eV	5.48	Ionization Energy , eV	3.6	Density , g/cm3	2.329
<input checked="" type="radio"/> Diamond	Electron Mobility , cm2/Vs	2534	Hole Mobility , cm2/Vs	1802	Electron sat. velocity , cm/s	13200000.0	Hole sat. velocity , cm/s	14200000.0
	Relative Permittivity	5.5						

Figure 4.8: The Sensor class dynamically creates the GUI (Sensor Properties) based on the sensor modelling it is assigned to represent.

Source Type	Alpha Properties	Laser Properties	MIP Properties
<input checked="" type="radio"/> Alpha	Alpha Energy (MeV): 5.5	Power avg , W: 0.1	Stopping Power , MeVcm2/g: 1.67
<input type="radio"/> Light	a/srim/IONIZ_He_on_Si_5.5MeV.txt	Pulse Duration , s: 45e-12	
<input type="radio"/> MIP	<input type="checkbox"/> Edit <input type="button" value="Open"/>	Wavelength , nm: 670	

Figure 4.9: The Source dialogue box, including separate parametrization for  $\alpha$ -particles, laser sources and MIP. An abstract charge distribution can also be added through the file input of the  $\alpha$  box.

of radiation sources provided. Each option was implemented in a separate class (for  $\alpha$ -particle, laser and MIP) and -contrary to what applied previously- every class had its own method of displaying the data due to the high variation in properties among the sources. In addition, instead of displaying only the selected object and deleting the rest from the layout, in this case the non-selected options are only disabled.

The **Electronics class** initializes multiple (3 in the case of *v2.2* of TCTsim) groups, each one of which represents different part of the read-out electronics (Fig.4.10). Each group contains a drop-down button which will determine the transient response of the chosen instrument. Therefore, corresponding classes (**Amplifier class**, **Cable class**, **Oscilloscope class**) contain the properties and parametrization of each element. As a result, a very detailed description of the electronics is possible through the designed mechanism, but as mentioned in the previous section this has not been yet fully exploited in the current version of the simulation.

The **Irradiation class** only contains information over the radiation dose absorbed by the detectors. In this class a implementation of the Hecht equation (Eq.3.31) and the charge lifetime (Eq.3.30) is included, removing drifting charge thus lowering the current pulses amplitude.

**Figure class** constitutes of a *Qt widget* containing a *matplotlib Figure* along with a *matplotlib NavigationToolbar*. Both the figure and the toolbar have been extended with functions and features that facilitate the procedure of plotting, displaying, comparing and importing/exporting data. The application contains 6 **Figure Class** widgets divided in 3 separate tabs, each one serving the plotting of a specific quantity. Therefore, the first tab displays the current pulse and the result after the effect of the front-end

## 4.2. TCT SIMULATION APPLICATION

Huber	Cividec 40dB	LeCroy 625Zi
Length , m: 0	BandWidth , MHz: 0, 2000	BandWidth , MHz: 0, 2500
Impedance , Ohm: 0	Rise Time , s: 180	Impedance , Ohm: 50
	Impedance , Ohm: 50	
	Gain , dB: 40	

Figure 4.10: The effect of any number of electronics can be introduced through the electronics group. Each element is described through separate classes which provides the parametrization.

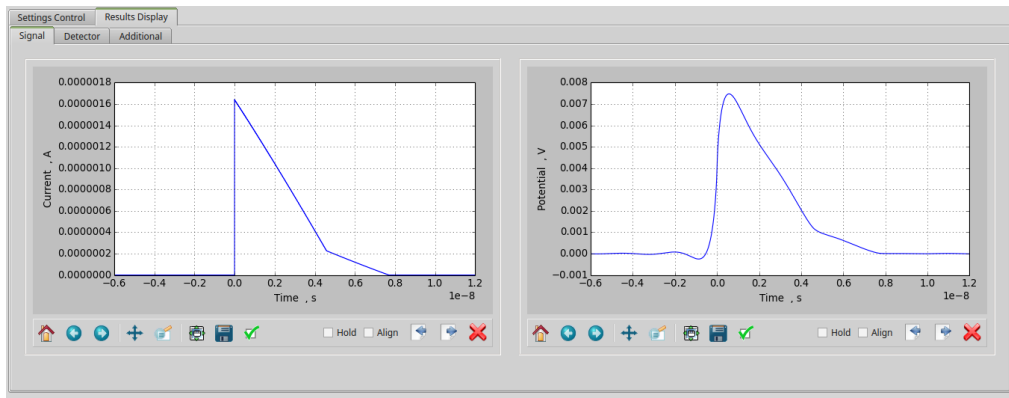


Figure 4.11: A figure widget has been implemented for the display of the results and introduced to the application in 6 separate instances describing different quantities.

electronics has been applied (Fig.4.11), the second tab contains information over the voltage, electric field and charge distribution in the detectors bulk and finally the last tab contains additional information such as the velocity of the carriers.

After the *Run* button is pressed, a **Worker class** thread initializes the **Model class** which then starts the calculation process. This design was preferred, as it offers the possibility of creating an interface for the **Model class** allowing the user to choose different implemented models. When initialized, the **Model class** accepts as arguments the instances of all the aforementioned quantities (classes), thus gathering all the settings and applying the algorithm.

Subsequently, as the algorithm suggests, the **PotentialField class**, **Charge class**, **DriftVelocity** calculate their corresponding values, while the **Calculation class** performs the main loop over time, and for each loop step the detector is iterated over its depth in order for the charge transport to be simulated.

Finally, the simulation concludes by displaying the results on the corresponding figure widgets.

### 4.3 Conclusions and Future Suggestions

Very complete simulations of the transient phenomena creating a current pulse already exist in literature [35], [36], [37] and they are under active development. The purpose of this simulation was primarily to familiarize the author to the semiconductor physics and then provide another platform which could serve as the basis for further development. Also, there was a clear focus on this work towards planar diodes and the modelling of the temperature dependence of the pulse's shape, elements of critical importance for the CryoBLM project. From that perspective, this application served its purpose.

Nevertheless, it is apparent that there are multiple features that the application lacks. An immediate evolution of the application would be to calculate the weighting and electric fields in 2-dimensional space. Moreover, diffusion or trapping effects are not being investigated in the current context. Additionally, the laser pulse radiation source should be considered as a Gaussian distribution which should be defined either by the corresponding  $\mu$  &  $\sigma$  parameters or by an arbitrary file. Similarly, the MIP radiation source could be expanded to simulate a beam of MIP particles. As already stated, in the current form of the application, the effects of the front-end electronics are simulated using a simple but valid approach. The application is designed in such a way, that in the ideal case a class describing the transfer function of each electronics element should be provided and its effect calculated. Last but not least, radiation damage effects such as the increase of depletion voltage and leakage current, but also the creation of trapping centres affecting the electric field distribution have not been included. Such analysis would require more time, investigation and information on areas which are still under ongoing research.

# Cryogenic Irradiation Experiment

## 5.1 Introduction

To investigate the radiation hardness of silicon and diamond detectors in cryogenic temperatures as well as their adequacy for LHC beam loss monitors, an irradiation experiment was conducted. The experiment took place from 5th of December, 2014, and lasted until early morning of 15th of December on the PS East Area.

The PS East Area is an experimental area at the PS accelerator containing four beam lines. More specifically, the experiment was located in the IRRAD irradiation facility. A plan of the facility can be seen in the Figure 5.1. The beam line of interest for the experiment is the T8. The T8 is a primary beam line which delivers primary protons to the irradiation facilities IRRAD and CHARM. [38] The beam properties are summarized in the Table 5.1 .

<i>Parameter</i>	<i>value</i>
Proton beam momentum [GeV/c]	24
Maximum # of protons per PS spill	$5 \cdot 10^{11}$
Maximum # of spills per super-cycle	6
Duration of super-cycle [s]	45.6
Minimum spot size [mm RMS]	$5 \times 5$
Beam spread (FWHM) at cryostat [cm]	1.2

Table 5.1: PS East Area T8 Beam Parameters [39].

The detectors used for the experiment were 2 *Si* pad diodes of similar design, a 3D *Si* and a 3D *sCVD* sample, and they are listed in the Table 5.2 along with their

## 5. CRYOGENIC IRRADIATION EXPERIMENT

---

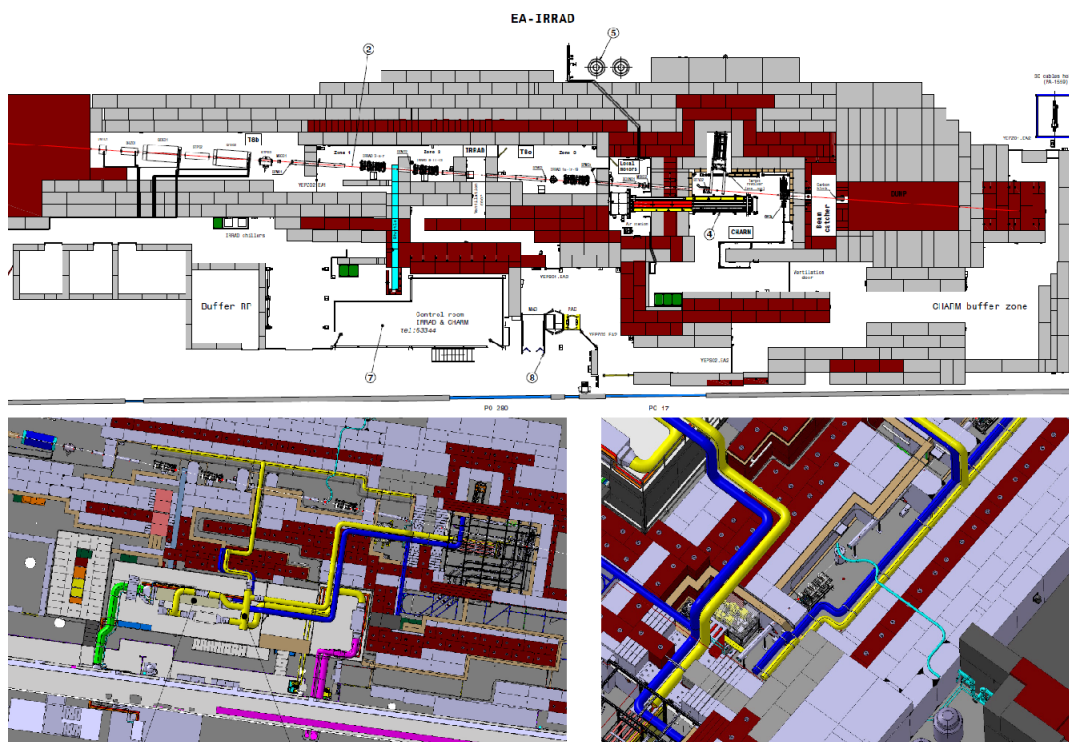


Figure 5.1: Plan of the IRRAD facility at the PS East Area. Image courtesy of Michael Lazzaroni.

properties (Fig.5.2). The detectors were placed inside a purpose-built cassette. In addition, two quadrant silicon detectors were placed at the two ends of the cassette for alignment purposes. The final set up of the cassette can be seen at the Figure 5.3. The cassette was placed inside a cryostat and cooled to a temperature of 4 K. Another silicon sample was placed outside of the cryostat for further study of damage after the end of the experiment along with two aluminium foils with size  $5 \times 5 \text{ mm}^2$  for total absorbed dose measurements.

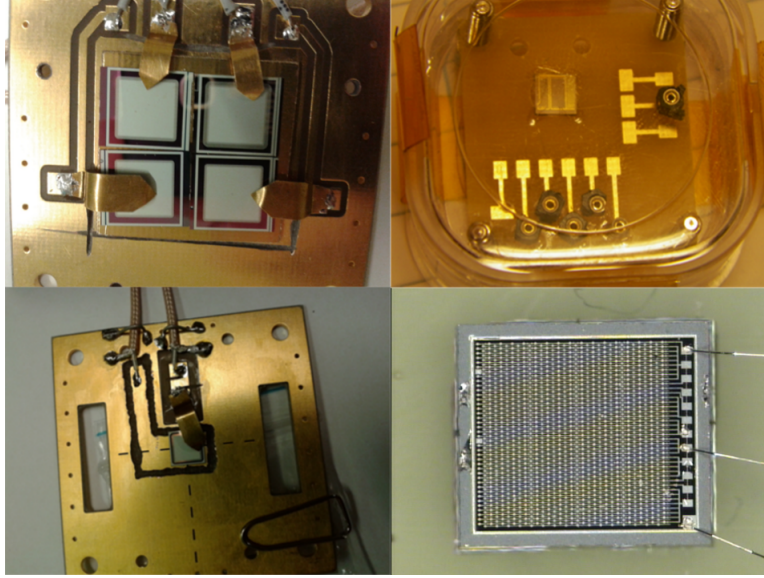


Figure 5.2: Images of (clockwise starting from upper left) the quadrant *Si* "beam telescope" detector, the  $500 \mu\text{m}$  *3D scCVD*, the *3D Si* and the  $300 \mu\text{m}$  *Si* (the  $100 \mu\text{m}$  *Si* had similar design). Images courtesy of Elena Verbitskaya (left) and Guilio Forcolin (right).

Insulated wires were soldered to all the detectors for the application of high voltage and the retrieval of the signal. All the detectors had one output signal while the diamond detector had two, first from the part of the detector with  $50 \mu\text{m}$  pitch of the 3D structure and second with  $150 \mu\text{m}$  pitch. Using the cabling infrastructure of the IRRAD facility, all the high voltage and signal cables reached the IRRAD control room patch panel, having a total length of approximately 40 meters. From the patch panel, BNC coaxial 10 ns  $50 \Omega$  cables were connected to four *Keithley 2410* high-voltage SourceMeters to bias the detectors and the signal was transferred through similar cables to the BLEDP stand-alone acquisition system.



## 5. CRYOGENIC IRRADIATION EXPERIMENT

---

<i>Detector</i>	<i>Active Area</i>	<i>Thickness</i>	<i>Resistivity</i>
Si	$5 \times 5 \text{ mm}^2$	$100 \mu\text{m}$	$10 \text{ k}\Omega\text{cm}$
Si	$5 \times 5 \text{ mm}^2$	$300 \mu\text{m}$	$10 \text{ k}\Omega\text{cm}$
3D Si	$3.5 \times 3.5 \text{ mm}^2$	$300 \mu\text{m}$	$10 \text{ k}\Omega\text{cm}$
3D sCVD	$3 \times 4 \text{ mm}^2$	$500 \mu\text{m}$	$100 \text{ TOhm}$ ( $100 \mu\text{m}$ )

Table 5.2: Detector samples used for the irradiation test.

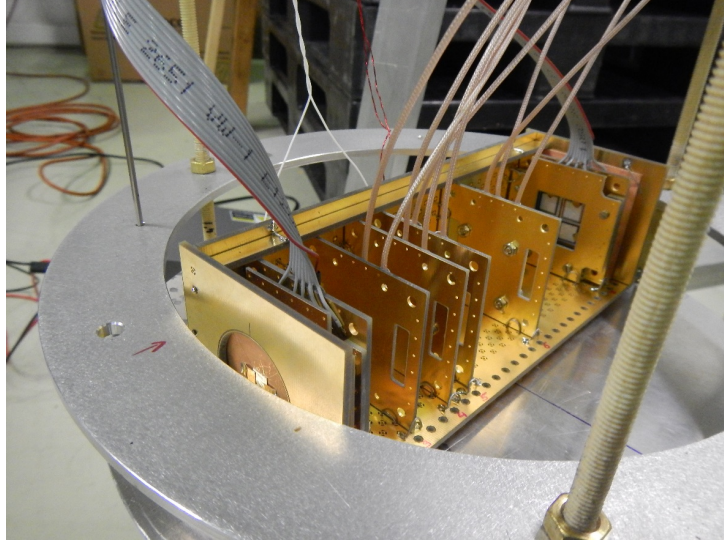


Figure 5.3: The cassette containing 3 Si and 1 sCVD samples plus the 2 quadrant Si. Image courtesy of Marcin Bartosik.



## 5.2 The BLEDP stand-alone acquisition system

### 5.2.1 The BLEDP Card

The BLM system is the main tool for beam setup and machine protection of the LHC. For the injector complex of the LHC, a new BLM system is currently under development. The purpose of the project is to provide faster measurements, higher dynamic range and compatibility with a variety of detectors used as input signal source, with positive or negative current polarity. The BLM system consists of the Acquisition Crate (BLEAC), the acquisition module (BLEDP) as well as further processing electronics. In parallel, a stand-alone measurement system is developed using the BLEDP acquisition module, both for assisting the development phases but also to later serve as an independent system [44]. An overview of the specification of the BLEDP readout card is provided in the Table 5.3.

To reach such a high dynamic range of  $2 \cdot 10^{10}$  a mixed measurement technique was implemented into a new acquisition card (BLEDP). This card operates with a combination of two measurement methods, the Fully Differential Frequency Converter (FDFC) and the Direct Analog Digital Converter (DADC). The two circuits have overlapping current measurement ranges, 10 pA – 10 mA for the FDFC and 100  $\mu$ A – 200 mA for the DADC. The switch between the circuits is handled by a FPGA with a required switch time of 100 ns. The BLEDP card can support up to 8 input channels. From the perspective of the CryoBLM experiment the BLEDP card is expected to operate only through the FDFC circuit, based on the expected signal amplitude from the detectors.

Furthermore, the FPGA is responsible for the majority of the control operations of the card. The start and stop of the acquisition, the pulses count during the acquisition period, the control of two digital potentiometers for the setting of the analogue comparator threshold and for the injection of an offset current of 2 nA, as well as the processing of the data are all handled by the FPGA. More information on the merging algorithm used to provide the processed data can be found in the literature provided [42]. In the standard configuration the system is expected to provide data

<i>Specification</i>	<i>Value</i>
Measurement range ( $> 6ms$ integration time)	10 pA to 200 mA
Error	$< \pm 10\%$
Minimum Integration Period	2 $\mu s$
Input range with minimum acquisition period	31 nA to 200 mA

Table 5.3: BLEDP acquisition system main specifications [43].

## 5. CRYOGENIC IRRADIATION EXPERIMENT

---

to the processing electronics through two point-to-point connections with bidirectional multi-gigabit optical links. [40]

Specifically for the stand-alone measurement system, the BLEDP card's FPGA was further exploited by embedding a soft-core CPU with a custom-made server. This system is connected to the network through Gigabit Ethernet and using the TCP/IP protocol, the server exposes the requested type of data. A communication protocol was developed for exchanging commands, collecting, storing and viewing different types of data [44]. For the needs of the experiment, this portable stand-alone BLEDP data acquisition system was used.



Figure 5.4: The front panel of the portable BLEDP stand-alone data acquisition system. Image courtesy of Christos Zamantzas.

### 5.2.2 BLEDP Communication Protocol

For the communication of the BLEDP card with a client software over the Ethernet link a protocol is provided. It specifies the commands that should be sent to the server process (implemented inside the FPGA in C programming language) as well as the data frame format transmitted to the client application.

Initially, the client must set up the connection with the server. This is performed via a standard three way TCP/IP handshake. Specifically for the stand-alone system, the IP address and port are hard coded to 192.168.137.10 : 30. The server is set to listen for a connection from a single client. For a single channel acquisition this TCP connection is used for the transfer of both the data and the status packages, while the multichannel acquisition is using a separate UDP port for the data due to the high bit rate. After

a successful connection, the server awaits for the command for the specification of the data desired by the client. The structure of the 7 byte command format is displayed in Figure 5.5 [41].

Start Stop	Data type	Channel number	Unused	Data Count	CRC
(1 bit)	(2 bits)	(3 bits)	(10 bits)	(32 bits)	(8 bits)

Figure 5.5: BLEDP command bit structure

As mentioned before the BLEDP card provides samples from each channel every  $2 \mu\text{s}$ . Every sample, from now on referred to as BLEDP frame, is 32 bits wide and contains a 6 bits header with information of the data type and the acquisition channel and a 26 bits data payload containing an incremental counter and the 20 bits acquired value. The structure of the BLEDP frame is displayed in the figure 5.4.

Acq / Status	Data type	Channel number	Increm. counter	Processed Data Value
(1 bit)	(2 bits)	(3 bits)	(6 bits)	(20 bits)

Figure 5.6: BLEDP processed data frame bit structure

Since the Ethernet MTU is 1500 bytes and in order to avoid IP fragmentation in any condition, the allowed payload was reduced and fixed to 1400 bytes for TCP single channel acquisition and 1408 bytes for multichannel, that is 350 and 352 BLEDP frames respectively. This package will be referred as BLEDP bundle. A graphical representation of the BLEDP bundle can be seen in figure 5.5. Consequently, for single channel acquisition a BLEDP bundle is received from the client every  $700 \mu\text{s}$ , while for multi channel the bundle is received every  $88 \mu\text{s}$  for a rate of around 16Mbps per channel.

### 5.2.3 Data Acquisition Application

A data acquisition client and data analysis software for the BLEDP card is already under development, written in the programming language Java. Despite the high level of this client, the application did not meet some of the experiments requirements. For this reason the author was assigned to implement another client application. The programming language of choice was Python, because of the authors familiarity and the fast development cycle usually provided based on the time constraints of the experiment.

## 5. CRYOGENIC IRRADIATION EXPERIMENT

---

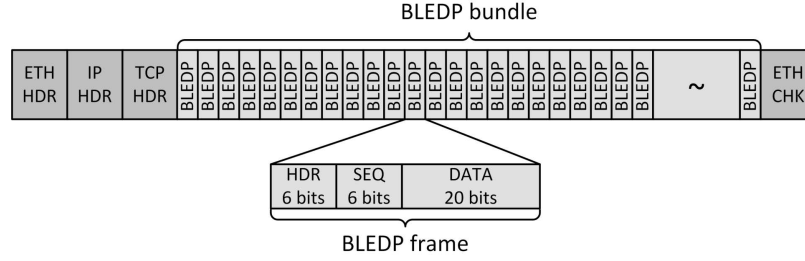


Figure 5.7: BLEDP bundle consists of 350 or 352 BLEDP frames for single or multi channel acquisition respectively

The design of the UI was done using the Qt framework, while other packages used for the development include matplotlib, numpy and scipy.

The application provided a graphical UI organized in two main windows, the client and the display (Fig. 5.8). Both the client and the display can run independently as a stand-alone applications. The client has the ability to initiate the display while the opposite is not possible. As expected, the online display option is enabled only if the display is initiated through the client.

The client application is responsible for the connection and communication of the client to the server as well as the acquisition and storing of the data and has been implemented with the following structure.

The **BledpGUI class** consists of the top level class, where the main interface of the client is initiated. The main window is divided in 5 parts each one serving a specific functionality (Fig. 5.9).

First, the connection must be set between the client and the server of the BLEDP card. Therefore, the **NetworkSettings class** is responsible for the interface and the value definition of all the parameters (IP, Port, UDP port). The default values are in agreement to the default values for the BLEDP stand-alone acquisition system expected values. In addition, a button is assigned with the execution of a connection attempt through the respective method in the **BledpClient class**. If the connection is not set, the data acquisition is not enabled and cannot be initiated.

Afterwards, the user encounters the channel selection menu implemented through the **ChannelSelection class**. The only purpose of this class is to provide the interface and store the selection of the user, so that the appropriate command based on the BLEDP protocol is sent to the server as discussed previously. As a result, single or multi channel acquisition is requested.

The third component of the client concerns the triggering functionality which was of great significance for the project as the client and the acquisition should be able to

## 5.2. THE BLEDP STAND-ALONE ACQUISITION SYSTEM

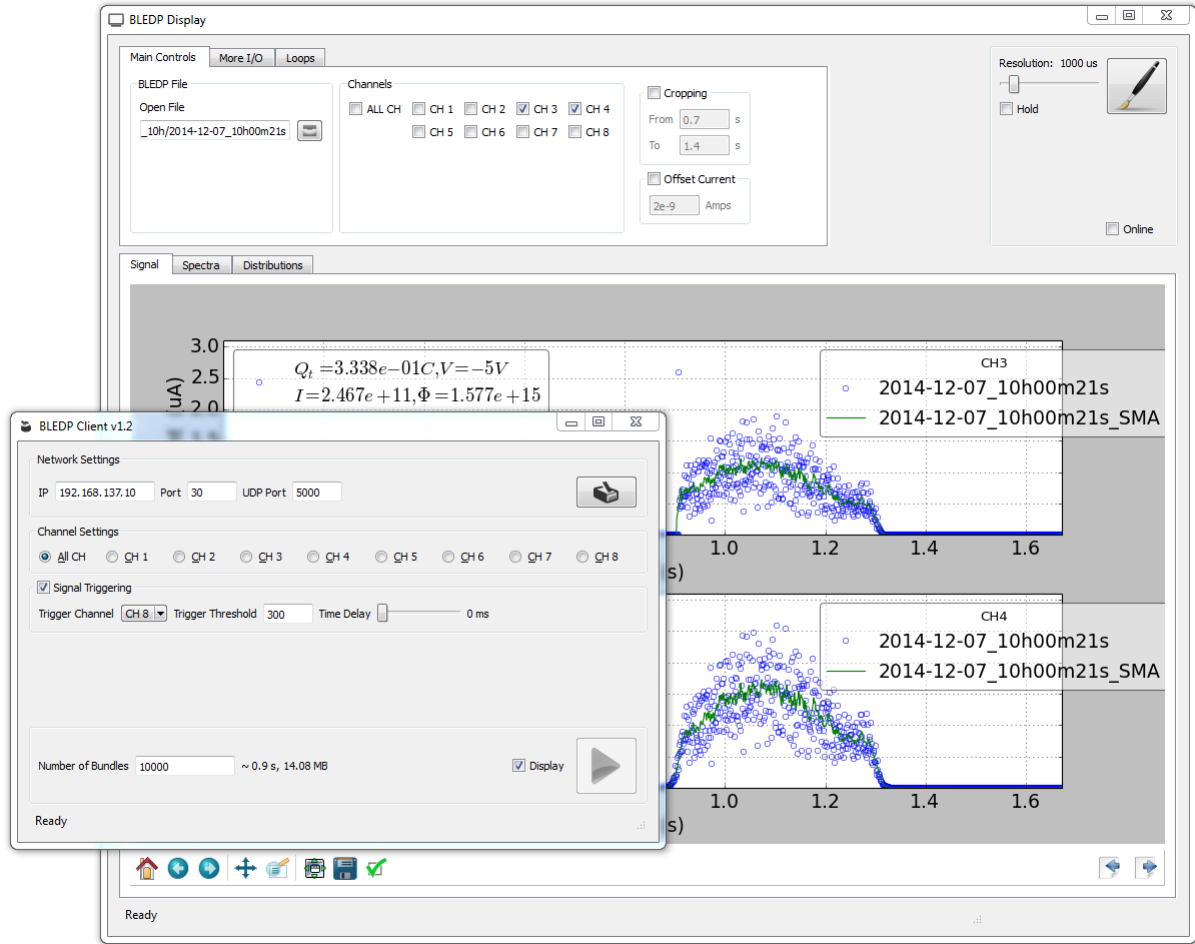


Figure 5.8: BLEDP Python client: the GUI of both independent windows of the application.

## 5. CRYOGENIC IRRADIATION EXPERIMENT

run unobstructed for a period of almost ten days. When enabled, the user could set the channel to listen for the trigger, the trigger's threshold and if desired a small delay (up to 800 ms)) before the acquisition is started. All the aforementioned settings are implemented in the **TriggerSettings** class.

As discussed in the BLEDP protocol section, the number of the desired bundles should be also set before sending the command to start the acquisition. For that purpose, the **BundlesSettings** is provided, enabling the user to set the number of bundles for the acquisition, while also displaying information on the duration and size of the acquired data based on the selection.

Last, the **RunBox** class initiates the acquisition based on the settings provided. The widget contains a button and a check box. The former starts the acquisition based on the settings while the other initiates the display window of the application. If the trigger functionality is not enabled simple single or multi channel acquisition is performed based on the channel selection. In a different case, the client will only listen to the channel selected from the trigger menu, and only when the threshold is exceeded single or multi channel acquisition is started. All the methods performing the acquisition loops are provided from the **BledpClient** class.

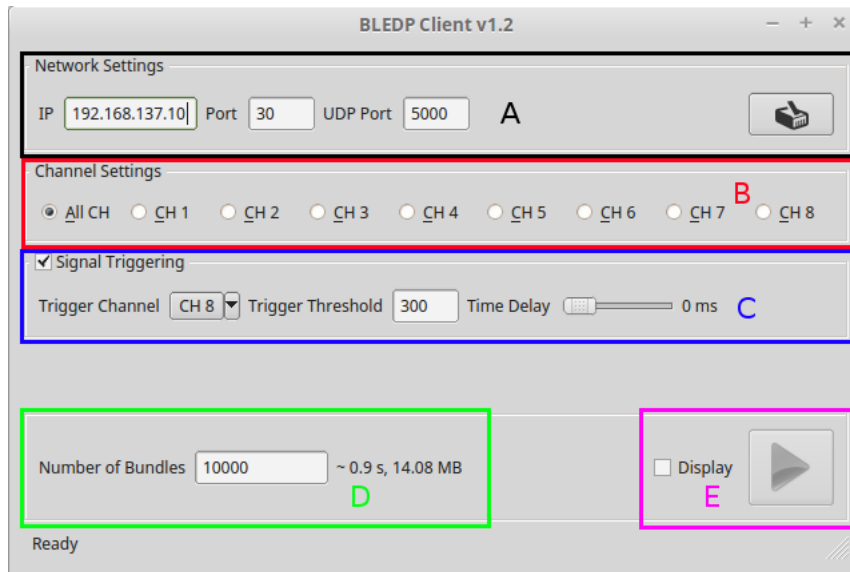


Figure 5.9: The GUI of the client window side of the application. The widget *A* is responsible for the connection setting of the client with the server. *B* and *D* are responsible for the definition of the command sent to the server assigned to commence the acquisition, while widget *C* controls the triggering functionality.

As above mentioned, the display can be run separately or through the client depending on whether the **BledpDisplay** class was initialized from the client window or separately. If is running though the client the display can be also set in online or offline mode.

The display window is divided in two tabbed components vertically aligned. In the top section, tabs containing the settings for the display or analysis of the data exist, while in the lower section there are tabs which include figures assigned to display the results. The settings consists of three tabs while the figure tabs are dynamically added or removed based on the selected settings.

When in online configuration most of the analysis functionality of the application is disabled. The plotting is controlled from the **BledpClient** class and it depends on the mode of the acquisition.

In offline mode all the analysis functionality is available to the user. This part of the application was developed during the data analysis, therefore it is suited for the needs of the investigation performed during and after the irradiation test.

The main controls tab of the application provides controls over the file selection (**OpenFile** class) and the channel selection (**ChannelSelection** class). Additionally, control over the display of the signal between specific moments and an option for the compensation of the offset current of the card have been added as options (Fig. 5.10).

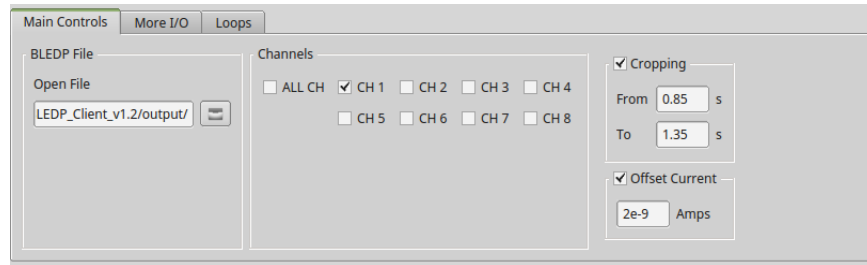


Figure 5.10: The main tab displaying the settings of the display window of the BLEDP client application.

The second tab of the settings concerns additional functionality regarding signal processing or retrieving of further information from separate files (Fig. 5.11). Hence, the **OptionsList** class includes several check boxes which act as boolean variables controlling what is sent to the figures for plotting. Similarly, the **AdditionalFiles** class contains multiple **OpenFile** class widgets which provide information on quantities such as e.g. beam position & intensity.

Looping over multiple files in order to extract results such as voltage scans and degradation curves is necessary in the context of this work. Therefore, such options are

## 5. CRYOGENIC IRRADIATION EXPERIMENT

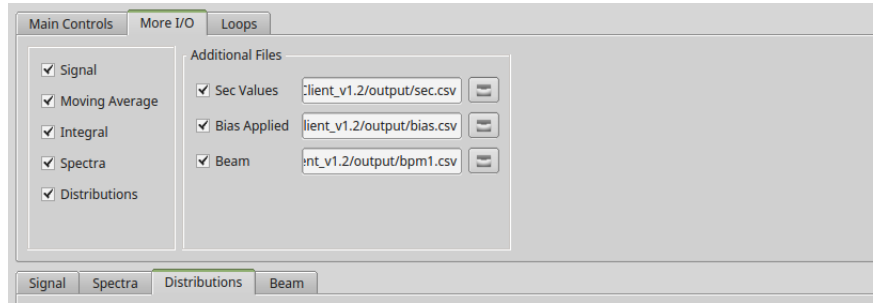


Figure 5.11: The additional options provided to the user in the second tab of the display window. Notice that for the spectra, distributions and beam parameters a separate tab containing a figure is created.

provided in the third tab of the settings (Fig. 5.12). If looping is enabled, the user can choose a dataset from a **OpenFilesDir** class widget and then proceed to the selection of the desired analysis. The choices offered in the current version of the application (v1.2) are plotting the collected charge as a function of time and fluence, plotting the mean signal as a function of time and plotting the collected charge in terms of the bias voltage applied. Furthermore, extracting csv files or images from a dataset or simply displaying the dataset in sequence is possible through the respective options. Last, the possibility to filter files based on some criteria was considered useful and is currently under development.

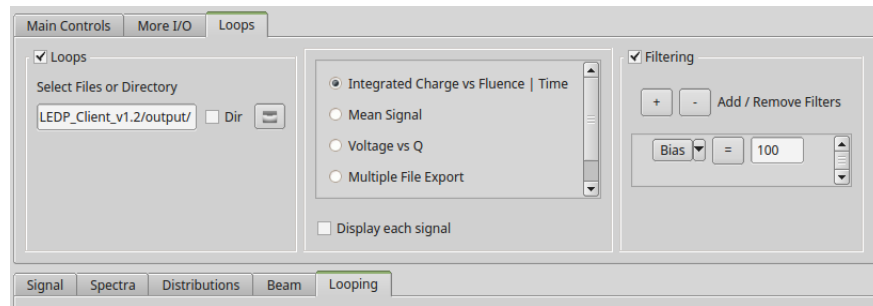


Figure 5.12: The third tab includes all the functionality provided for looping through multiple files. Degradation curves and voltage scans are created through this process. Note that the results are plotted in a dedicated figure tab.

Finally, the figures of the lower tabs are **Figure** class widgets (also used and mentioned in TCTsim application) which provide a modular and well structured interface



## 5.2. THE BLEDP STAND-ALONE ACQUISITION SYSTEM

for plotting the results while also including a specific protocol for importing and exporting files and data. As an example, in Figure 5.13 an example signal output of the *Keithley 6430* current source is provided, along with the its distribution.

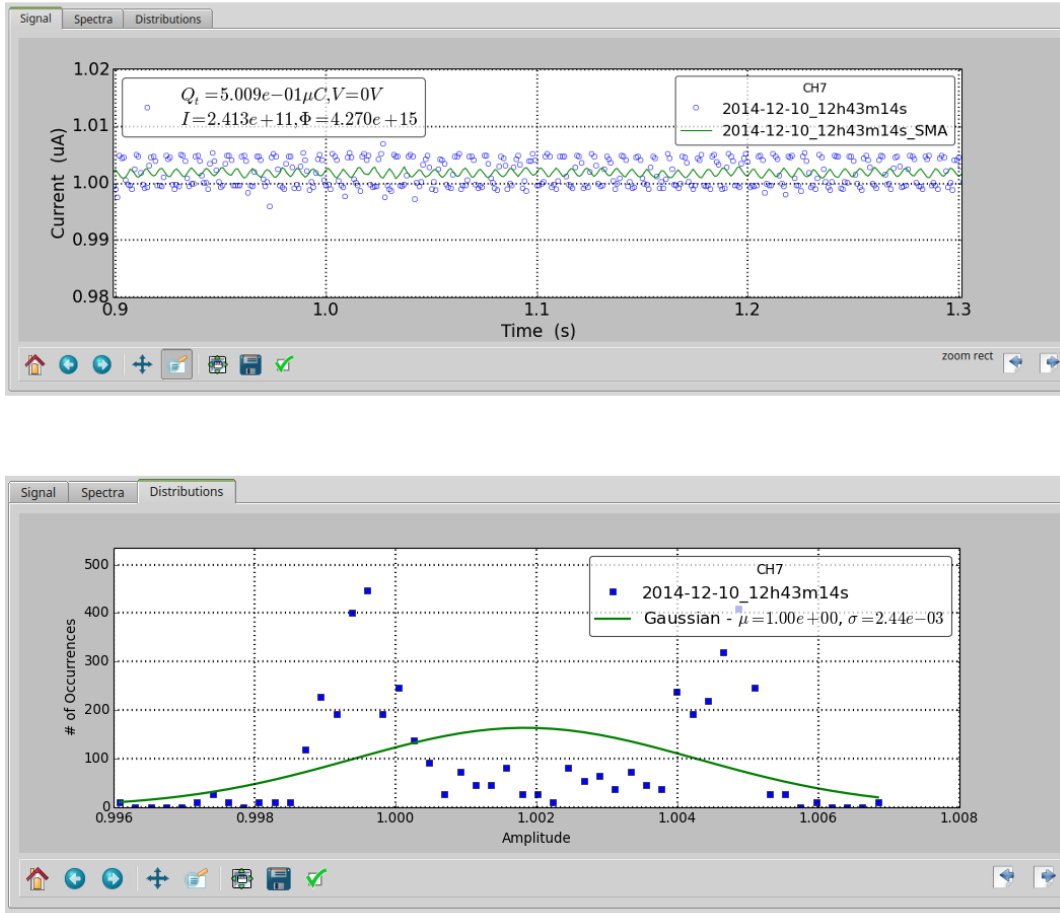


Figure 5.13: Example of plots displayed by the figure widgets of the BLEDP client display window. First, the data with a line representing a simple moving average, while on the second plot their distribution with a gaussian fit is shown.

### 5.3 Data Analysis

During the irradiation test, the BLEDP system with the aforementioned client were used to collect the signal data from the detectors. By the end of the experiment the responses for  $\approx 28.000$  spills have been recorded and saved for offline analysis from all four detectors.

Table 5.4 shows the settings and assignments like detector bias votages and channel definitions of the BLEDP card. The 6th channel of the card has been empty for the first days of the test, and later one signal output from the front quadrant silicon detector was connected.

Additionally, a *Keithley 6430* current source was connected to 7th channel of the card for calibration purposes. The current source was set to  $0.5 \mu\text{A}$  or  $1 \mu\text{A}$  in different occasions, and was connected to all the BLEDP channels to verify the correct operation of the card. Finally, the resulting calibration coefficient for the conversion of the bit value to current was calculated to be  $15.675 \text{ bits}/\mu\text{A}$  taking under consideration also the  $2 \text{ nA}$  offset current of the card.

Finally, the trigger signal has been connected in the 8th channel. The client was set to trigger mode, with the trigger threshold level set to 300 bits, that corresponds to  $\approx 1 \text{ mV}$  taking under consideration the aforementioned coefficient and the cards  $50 \Omega$  input resistivity.

<i>Detector</i>	<i>Bias</i>	<i>BLEDP Channel</i>
$100 \mu\text{m Si}$	$-100 \text{ V}$	<i>CH1</i>
$300 \mu\text{m Si}$	$100 \text{ V}$	<i>CH2</i>
$3D \text{ Si}$	$-5 \text{ V}$	<i>CH3</i>
$3D \text{ sCVD}$	$\pm 100 \text{ V}$	<i>CH4 &amp; CH5</i>

Table 5.4: Detectors standard bias voltages used and assignments of the BLEDP card.

#### Beam shape & intensity

The beam shape and size has been defined for every collected spill based on the BPM data. More specifically, in the context of this work, the data used were the gaussian fit coefficients for both planes from the BPM1 strip detectors which are placed  $20 \text{ m}$  upstream of the cryostat's location. The data are displayed in Fig.5.14, with significant variation only observed in the *x-axis* of the beam's position.

Similarly, the intensity of each spill was collected from secondary emissions monitor counts data. The values were multiplied by a calibration value of  $1.4 \cdot 10^7 \text{ protons/count}$

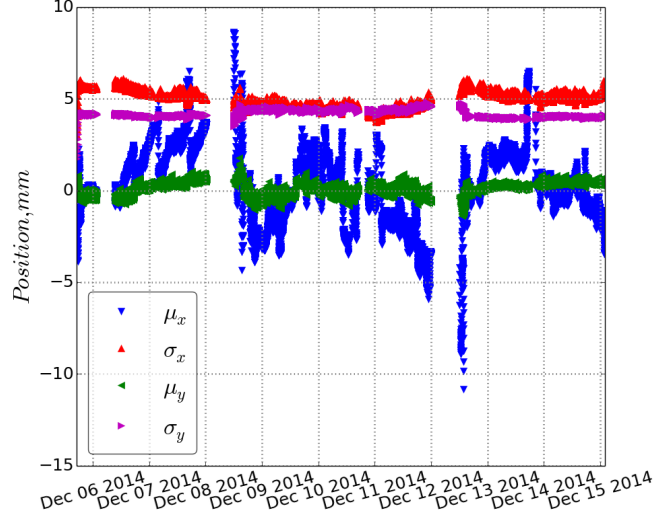


Figure 5.14: Beam position measurements for the whole irradiation period. The presented data have been averaged over 10 values.

resulting to the estimated number of protons. As can be observed in Fig.5.15, the mean value of the beam intensity was  $2.36 \cdot 10^{14}$  protons per spill, with a variation of  $\approx 5\%$ .

Based on the aforementioned datasets, an estimation of the beam shape and intensity could be derived for each collected signal. A depiction of a beam intensity distribution in space based on the mean values of the beam parameters is shown in Fig.5.16. For every spill, a similar reconstruction of the beam is created and the absorbed dose by each detector is defined by integrating the reconstructed beam within the limits of the detectors size (Table.5.2). Hence, through this calculation process, results for the beam intensity of each spill and for the fluence absorbed have been provided.

It should be noted, that after the end of the irradiation test, the total fluence has also been measured using the aluminium foils activation, which as mentioned earlier were placed outside of the cryostat. Protons induce nuclear reactions in the aluminium foils with the consequent production of unstable nuclides. The activity of these nuclides ( $Na-22$  in this particular case) is measured with  $\gamma$  spectrometry and then the number of protons that induced this activity in the sample is estimated [45]. The resulting values were  $7.085 \cdot 10^{14}$  protons which is just 54% of what was calculated by the previously mentioned process. The intensity data were normalised to match the dose measurement results as the activation method has a higher accuracy compared to the beam position reconstruction method.

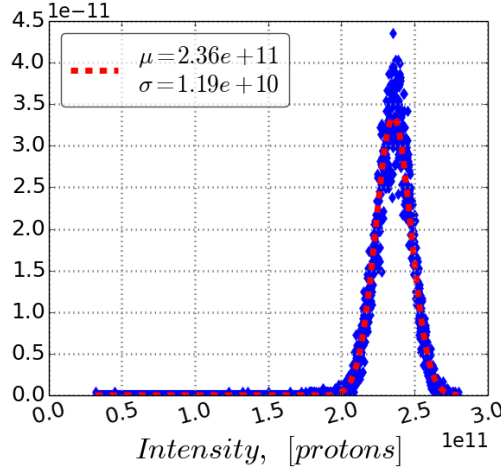


Figure 5.15: Distribution of the beam intensity values as collected from the SEC data.

### Signal data collection

As previously mentioned, a large number of spills has been recorded throughout the irradiation test. The multichannel acquisition time was set to 1.672 s stored in files of 25.6 MB size, thus resulting in over 700 GB total amount of data. A sample of the signal response for all the detectors is depicted in Fig.5.17. The full data set taken during the irradiation test is still subject of further comprehensive analysis. In consequence, the following description of the data analysis procedure and the results are representing the current state of it.

Moreover, the data should be considered with caution for the following additional reasons. Primarily, during the first 28 hours of irradiation -that is fluence of up to  $\sim 5 \cdot 10^{14}$  protons-, compliance settings of the voltage sources were in some cases significantly limiting the detector's response, thus making the data inappropriate for CCE observations and conclusions. Also, the two Si detectors were floating, and a source of noise whose origin is still unclear was introduced. Furthermore, after the retrieval of the detectors from the cryostat, it has been observed that one of the electrodes of the *scCVD* has failed and therefore making the corresponding results non credible. Last, the estimation for the protons passing the detectors for each spill as explained before, is still a subject of investigation. The BPM used for the analysis was not close to the cryostat, and the correction applied for the CCE determination often seemed to over-correct the data.

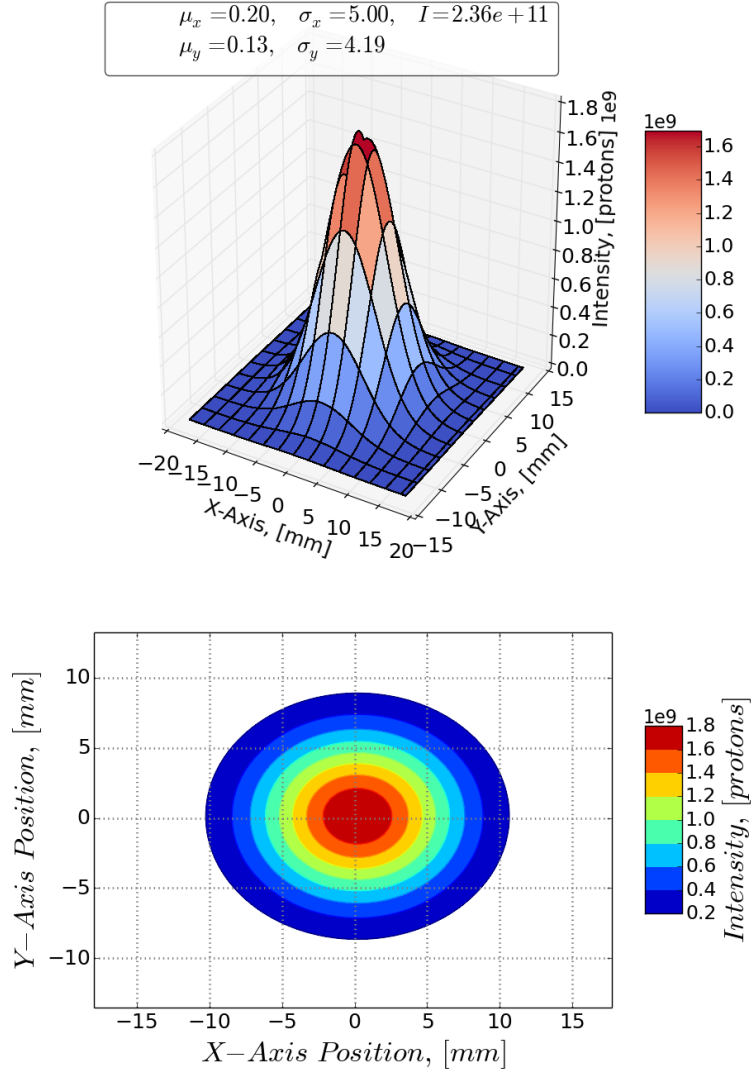


Figure 5.16: Intensity distribution in space of the beam based on the data from BPM1 and SEC. A representation of the beam was created for each spill to calculate the dose accepted of each sensor.

## 5. CRYOGENIC IRRADIATION EXPERIMENT

---

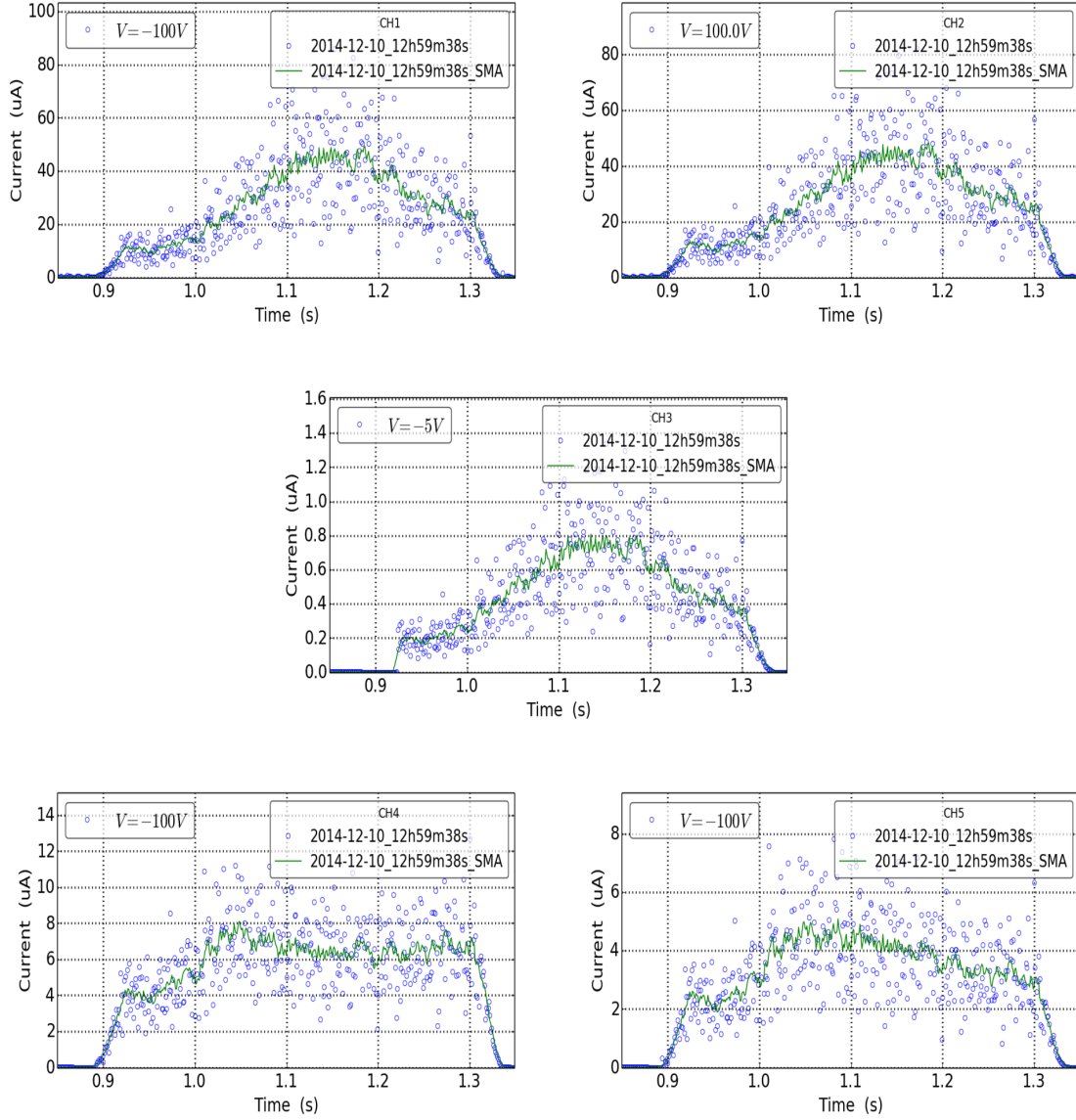


Figure 5.17: Signal currents as function of spill time for all irradiated detectors. The blue circles represent the data returned from the card averaged over 1 ms (500 *points*) and the green line is a simple moving average of the data.

### Degradation Curves

A representation of the CCE degradation of the detectors can be observed in Figure 5.18. The 300  $\mu\text{m}$  *Si* detector and the *scCVD* curves start after the change of the voltage source setting as they were affected significantly. Similarly, the small increase of the CCE of the 100  $\mu\text{m}$  *Si* detector observed at the same time could be caused by the same reason. In addition, the data retrieved from the 50  $\mu\text{m}$  side of the *3D scCVD* detector require further study in order to reach to conclusions and they have been omitted.

The degradation of the CCE of the detectors has been investigated and the current results can be summarized as follows:

- The 100  $\mu\text{m}$  *Si* detectors CCE degrades by approximately a factor of ten comparing initial to final CCE up to a maximum fluence of  $7 \cdot 10^{14}$ .
- Similarly, starting from  $\Phi \approx 6.5 \cdot 10^{13}$ , the 300  $\mu\text{m}$  *Si* detectors CCE seems to be halved. The larger 300  $\mu\text{m}$  detector seems to be more sensitive to trapping thus creating the same amount of charge as the thinner 100  $\mu\text{m}$  in fluences around  $10^{14}$  protons.
- The *3D Si* data span in fluence from  $\Phi = 3.3 \cdot 10^{11}$  to  $\Phi = 3.2 \cdot 10^{14}$ , during which period the CCE of the detector has decreased by more than two orders of magnitude.
- The *3D scCVD* has also degraded from  $\approx 0.4$  to 0.06 fC/MIP between  $\Phi = 6.5 \cdot 10^{13}$  and  $\Phi = 3.3 \cdot 10^{14}$ .

Last, a fit based on the equations presented in chapter 3.3 (equations 3.30, 3.31) is displayed in Figure 5.19. The fit was calculated having as free parameters the damage coefficient  $k$  and the  $s$  parameter. Although this plot is provided with precaution as further investigation is required, it seems that the parametrization is fitting well the degradation curves.

## 5. CRYOGENIC IRRADIATION EXPERIMENT

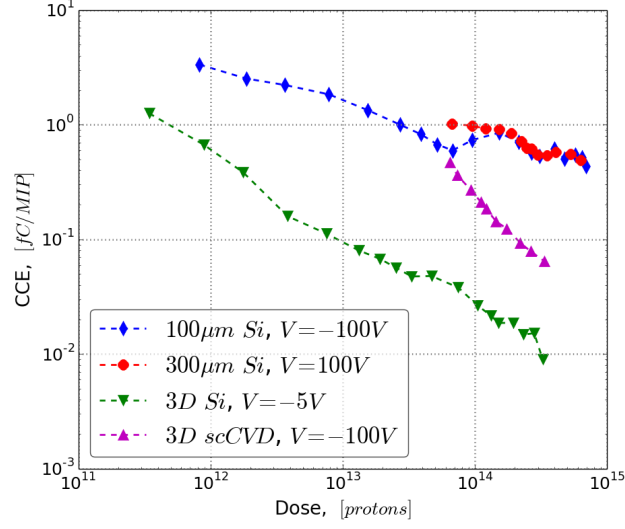


Figure 5.18: Degradation of the CCE of all four irradiated samples. The presented curves were based on beam shape data from BPM1 with a considered alignment of the cassette of  $-1.7$  mm. Moreover, the intensity of each spill has been normalized such as to match the aluminium foil fluence measurement.

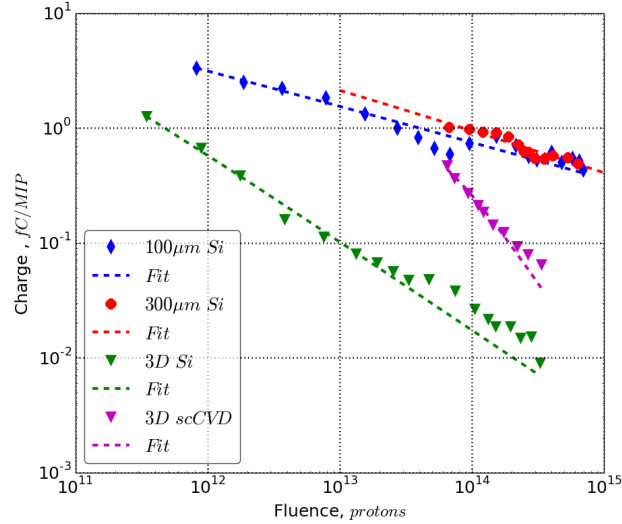


Figure 5.19: Fit of the CCE data based on the formulas presented in section 3.3.



### Voltage Scans

The dependence of CCE to voltage levels was investigated by voltage scans performed at three different fluences on 09/12, 13/12 and 14/12. The curve shapes were similar to the previously performed irradiation test [5]. The collected charge increased with the increasing voltage, and showed a tendency to saturation.

In the two *Si* pad detectors operated as charge injection devices (CIDs), i.e at forward (positive) bias, the increase was more apparent and the collected charge was larger than in reverse bias (Fig.5.21). This is caused by the reduction of the effective trap concentration due to filling via carrier injection. The advantage of CIDs is that they can achieve effective operation at lower voltages [46].

The *3D Si* has demonstrated a steady degradation of the CCE as seen in Fig.5.18 and this is also observed in the voltage scans (Fig.5.20). The CCE in  $\Phi = 3.11 \cdot 10^{14}$  is approximately half compared to the first voltage scan at  $\Phi = 1.23 \cdot 10^{14}$ .

Last, the voltage scans of the *3D scCVD* are displayed in Fig.5.22. The detector had a significant increase in collected charge when operated with negative bias. Curiously, the  $50 \mu\text{m}$  pitch side of the detector collected less charge in negative bias during the first voltage scan, while the following two voltage scans demonstrated the expected degradation.

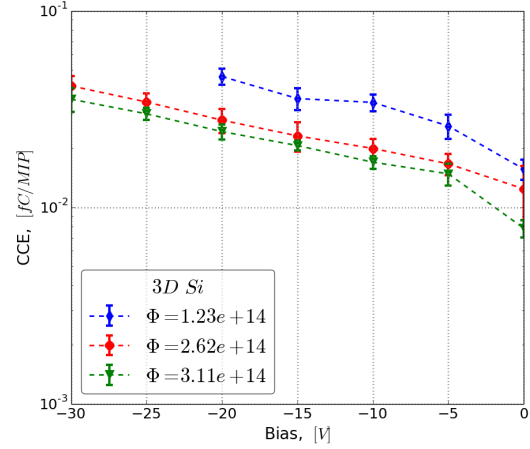


Figure 5.20: Voltage scans of the  $300 \mu\text{m}$  *3D Si* detector.

## 5. CRYOGENIC IRRADIATION EXPERIMENT

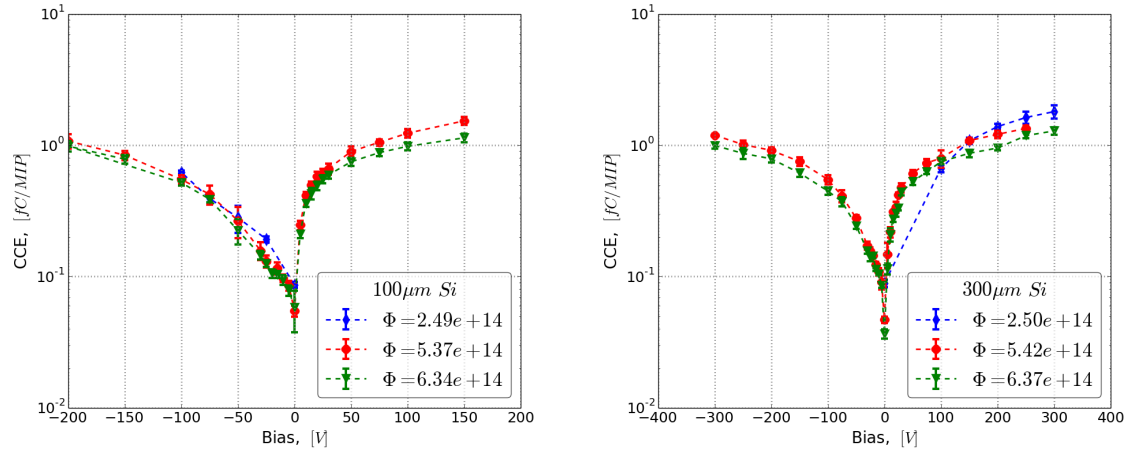


Figure 5.21: Voltage scans of the two *Si* pad diodes of 100  $\mu\text{m}$  and 300  $\mu\text{m}$  thickness.

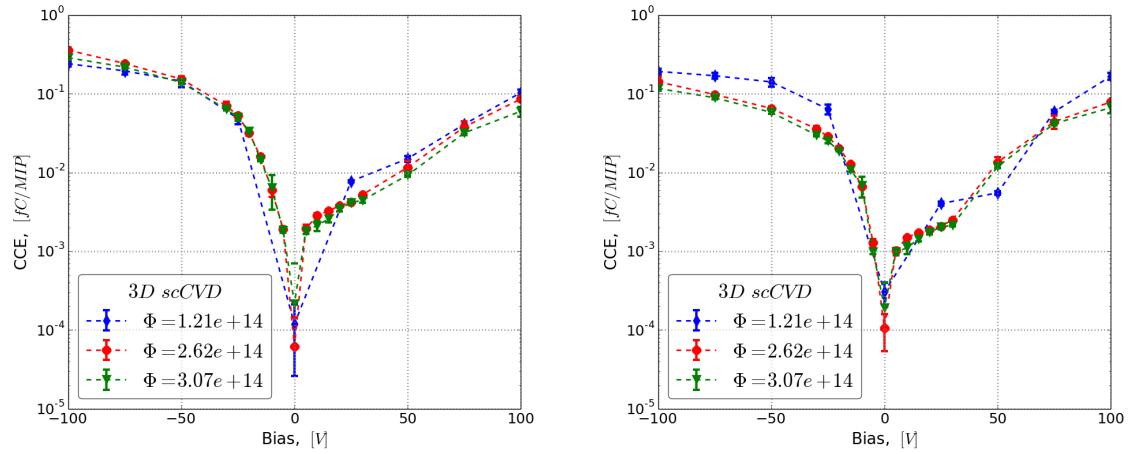


Figure 5.22: Voltage scans of the 500  $\mu\text{m}$  3D scCVD for the 50  $\mu\text{m}$  (left) and the 150  $\mu\text{m}$  (right) pitch sides.

## 5.4 Conclusions and Future Suggestions

The *in situ* irradiation test in 12/2014 confirmed previous results and showed the possibility of the solid-state detectors to operate in harsh radiation environment at 1.9 K. It has been shown that current injection, which has been developed as a tool for increasing the tolerance of silicon detectors to irradiation at moderate cooling, is still effective at 1.9 K.

In addition, the test provided with some very useful technical conclusions. First, the BLEDP stand-alone acquisition system proved to be a very modular, reliable system capable of acquiring signals in a very high frequency. The designed client also performed very well, as the triggering system performed autonomously and reliably, capturing  $\approx 75\%$  of the spills.

Of course, there were a few issues which are already noted for the forthcoming irradiation test in 11/2015. First, there is the need for more precise BPM data, closer to the cryostat. This has been already addressed, and a BPM will be exactly in front of the cryostat, providing the most accurate data possible for the beam position and shape. The dependence of the protons absorbed by the sensor to the detectors signal is significant and its sensitivity should be investigated. Furthermore, both the Gaussian fit and the raw BPM data should also be taken into account, especially when the beam is unstable. Additionally, voltage scans should be performed in a daily basis, ideally through an automated application (under development) for logging and controlling the *Keithley* voltage sources. Consequently, degradation curves for multiple voltage levels can be deducted. Last, a system logging the temperature of the cryostat should be included so that leakage current dependence to the temperature can be measured.

## Conclusions

The major goal of this work is to investigate the adequacy of using semiconductor detectors as BLMs inside the cold mass of the magnets, in cryogenic temperatures.

First, a research of transient phenomena in semiconductor detectors focusing on the temperature effects was carried out, giving an understanding of semiconductor physics to the author. In chapter 3, the result of this study is presented, which formed the basis of the next project. The TCTsim application (chapter 4) was developed with the purpose of providing a fast way to assess the shape of the pulse caused by radiation sources in a semiconductor detector. As there is still a significant ongoing research on the subject, the application has been designed in a modular and flexible manner, so that further modelling can be easily applied. The materials covered in this version (v2.2) are silicon and diamond, and the radiation sources include  $\alpha$ -particles, laser sources and MIP.

Subsequently, as part of the preparation for the scheduled irradiation test (12/2014), the author was assigned to develop a client application for the BLEDP stand-alone data acquisition system. The application should be able to acquire, store and display the recorded signals. Further challenges included the very high data rate ( $\sim 16$  MBps), the triggering functionality and the high reliability required, so that ten days of continuous operation could be achieved. The client application served its purpose providing a large amount of data for analysis.

The main goals for the analysis were to examine the degradation of the charge collection efficiency of the irradiated detectors, and additionally review their dependence on bias voltage and beam shape. All the required procedures for the extraction of these information were also added to the functionality of the client application display window, which was further developed to work independently and perform offline analysis. Hence, similar investigation needed for the forthcoming irradiation test will be more

---

efficient.

The outcome of the analysis confirmed previous results, and showed that semiconductor detectors operate well in cryogenic temperatures, meeting the challenges of the project and displaying their performance as a fast detection system. Still, due to difficulties encountered during the irradiation test, further investigation is needed and the repetition of the experiment (11/2015) will provide an even better insight.

# List of Tables

2.1	Energy stored in LHC magnets considering operation at nominal beam energy of 7 TeV [8]. . . . .	7
2.2	Challenges of the LHC BLM system. . . . .	8
3.1	Basic properties of Silicon and Diamond detector materials. . . . .	23
5.1	PS East Area T8 Beam Parameters [39]. . . . .	45
5.2	Detector samples used for the irradiation test. . . . .	48
5.3	BLEDP acquisition system main specifications [43]. . . . .	49
5.4	Detectors standard bias voltages used and assignments of the BLEDP card. . . . .	58

# List of Figures

1.1	CERN's logo and member states as of June 2015. . . . .	2
1.2	CERN's Accelerator Complex. . . . .	3
1.3	The Proton Synchrotron Complex. . . . .	4
2.1	An overview of the LHC MPS. Each subsystem can request beam dump through the BIS. Almost 4000 devices are installed as part of the BLM system. The BLM system is the only system to prevent magnet quenches and the main system to prevent magnet damage from multi-turn beam losses. . . . .	9
2.2	A description of the relation between the protection system engagement and the duration of the beam losses. . . . .	9
2.3	The Ionization Chambers used for the LHC Beam Loss Monitor system and their position in the quadrupole magnets of the arc [6]. . . . .	10
2.4	1) Deposited dose in the coils from losses inside the second quadrupole magnet, 2) Deposited dose in the coils from the debris, 3) BLM signal from debris (one cross for each BLM), 4) BLM signal from dangerous losses inside Q2B, 5) Proposed BLM beam abort threshold to protect from dangerous losses. One can see that the debris can mask the signal from a dangerous loss and that the proposed threshold is not adequate [5].	12
2.5	Layout of the detectors on the cold mass surface of Main Dipole magnets.[9].	13
2.6	A representation of the bunch-by-bunch resolution of a diamond BLM compared to the existing ionization chambers [4]. . . . .	14
3.1	Stopping power of positive muons in copper as a function of $\beta\gamma$ and momentum. The region described by Bethe is marked, and the effect of the density effect in high energies is also presented. . . . .	17

## LIST OF FIGURES

---

3.2	The PDF of Landau distribution with the most probable value ( $\Delta p$ ), and the mean rate of energy loss ( $-dE/dx$ ) quantitatively placed. . . . .	17
3.3	Most probable energy loss in silicon, scaled to the mean loss of a MIP [25].	18
3.4	Stopping Power at minimum ionization for different chemical elements. For $Z > 6$ a fit as of $-\ln(Z)$ is depicted. A simple functional dependence on $Z$ is not to be expected, since stopping power also depends on other variables [25]. Silicon and Carbon have an atomic number of $Z = 14$ and $Z = 6$ respectively. . . . .	19
3.5	$\alpha$ -particle range in <i>Si</i> & <i>C</i> and their respective Bragg curve displaying the energy deposition inside the target material. . . . .	20
3.6	Charge creation from laser source of different wavelengths inside the bulk of a <i>Si</i> detector. . . . .	22
3.7	At high temperatures or with a low $E_g$ electrons can reach the conduction band. . . . .	23
3.8	A schematic diagram of the electric field pattern inside a partially depleted irradiated silicon detector. The width of the high electric field region adjacent to the $p^+$ side may be quite small [17]. . . . .	26
3.9	Temperature dependence of the carrier mobility in Si and CVD. . . . .	27
4.1	$\alpha$ -TCT with $^{241}\text{Am}$ on a sCVD sample acquired from a 2.5GHz oscilloscope. This test was not performed in vacuum, so energy loss due to the 3 mm air layer between source and detector should be taken into account.	35
4.2	A typical TCT setup. Illumination of the detector from different sides with a laser source induces current mostly contributed from one type of charge carrier. Modified from [30]. . . . .	35
4.3	A block diagram of the algorithm implemented for the signal formation.	39
4.4	The main window of the TCTsim application. From the first tab, the user can select and alter options related to the detector material properties, the radiation source type as well as simulation factors such as bias, temperature or sample frequency. . . . .	40
4.5	Python along with PyQt, Numpy and Matplotlib were used for the development of the TCTsim application. . . . .	40
4.7	The SimControl widget contains the data and options of the displayed parameters. . . . .	41
4.6	The "Run box" is part of the SimControl widget. . . . .	41
4.8	The Sensor class dynamically creates the GUI (Sensor Properties) based on the sensor modelling it is assigned to represent. . . . .	42



4.9	The Source dialogue box, including separate parametrization for $\alpha$ -particles, laser sources and MIP. An abstract charge distribution can also be added through the file input of the $\alpha$ box. . . . .	42
4.10	The effect of any number of electronics can be introduced through the electronics group. Each element is described through separate classes which provides the parametrization. . . . .	43
4.11	A figure widget has been implemented for the display of the results and introduced to the application in 6 separate instances describing different quantities. . . . .	43
5.1	Plan of the IRRAD facility at the PS East Area. Image courtesy of Michael Lazzaroni. . . . .	46
5.2	Images of (clockwise starting from upper left) the quadrant <i>Si</i> "beam telescope" detector, the $500\ \mu\text{m}$ <i>3D scCVD</i> , the <i>3D Si</i> and the $300\ \mu\text{m}$ <i>Si</i> (the $100\ \mu\text{m}$ <i>Si</i> had similar design). Images courtesy of Elena Verbitskaya (left) and Giulio Forcolin (right). . . . .	47
5.3	The cassette containing 3 <i>Si</i> and 1 <i>scCVD</i> samples plus the 2 quadrant <i>Si</i> . Image courtesy of Marcin Bartosik. . . . .	48
5.4	The front panel of the portable BLEDP stand-alone data acquisition system. Image courtesy of Christos Zamantzas. . . . .	50
5.5	BLEDP command bit structure . . . . .	51
5.6	BLEDP processed data frame bit structure . . . . .	51
5.7	BLEDP bundle consists of 350 or 352 BLEDP frames for single or multi channel acquisition respectively . . . . .	52
5.8	BLEDP Python client: the GUI of both independent windows of the application. . . . .	53
5.9	The GUI of the client window side of the application. The widget <i>A</i> is responsible for the connection setting of the client with the server. <i>B</i> and <i>D</i> are responsible for the definition of the command sent to the server assigned to commence the acquisition, while widget <i>C</i> controls the triggering functionality. . . . .	54
5.10	The main tab displaying the settings of the display window of the BLEDP client application. . . . .	55
5.11	The additional options provided to the user in the second tab of the display window. Notice that for the spectra, distributions and beam parameters a separate tab containing a figure is created. . . . .	56
5.12	The third tab includes all the functionality provided for looping through multiple files. Degradation curves and voltage scans are created through this process. Note that the results are plotted in a dedicated figure tab. . . . .	56

## LIST OF FIGURES

---

5.13	Example of plots displayed by the figure widgets of the BLEDP client display window. First, the data with a line representing a simple moving average, while on the second plot their distribution with a gaussian fit is shown. . . . .	57
5.14	Beam position measurements for the whole irradiation period. The presented data have been averaged over 10 values. . . . .	59
5.15	Distribution of the beam intensity values as collected from the SEC data. . . . .	60
5.16	Intensity distribution in space of the beam based on the data from BPM1 and SEC. A representation of the beam was created for each spill to calculate the dose accepted of each sensor. . . . .	61
5.17	Signal currents as function of spill time for all irradiated detectors. The blue circles represent the data returned from the card averaged over 1 ms (500 <i>points</i> ) and the green line is a simple moving average of the data. . . . .	62
5.18	Degradation of the CCE of all four irradiated samples. The presented curves were based on beam shape data from BPM1 with a considered alignment of the cassette of $-1.7$ mm. Moreover, the intensity of each spill has been normalized such as to match the aluminium foil fluence measurement. . . . .	64
5.19	Fit of the CCE data based on the formulas presented in section 3.3. . . . .	64
5.20	Voltage scans of the $300\text{ }\mu\text{m}$ 3D <i>Si</i> detector. . . . .	65
5.21	Voltage scans of the two <i>Si</i> pad diodes of $100\text{ }\mu\text{m}$ and $300\text{ }\mu\text{m}$ thickness. . . . .	66
5.22	Voltage scans of the $500\text{ }\mu\text{m}$ 3D scCVD for the $50\text{ }\mu\text{m}$ (left) and the $150\text{ }\mu\text{m}$ (right) pitch sides. . . . .	66

# Bibliography

- [1] CERN's homepage, "www.cern.ch"
- [2] Beam Instrumentation Group website, "https://espace.cern.ch/beamdep/BI/default.aspx"
- [3] Wikipedia, the free encyclopedia, "www.wikipedia.org"
- [4] Rhodri Jones, *Introduction to LHC Beam Instrumentation*, CERN Academic Lectures 2014
- [5] Cristoph Kurfurst, *Cryogenic Beam Loss Monitoring for the LHC*, CERN-THESIS-2013-232, CERN, Geneve, 2013.
- [6] Bernd Dehning et al., *The LHC Beam Loss Measurement System*, Proceedings of PAC07, Albuquerque, New Mexico, USA, 2007
- [7] Eva Barbara Holzer et al., *Beam Loss Monitoring for LHC Machine Protection*, Technology & Instrumentation in Particle Physics 2011
- [8] R. Schmidt et al., *Protection of the CERN Large Hadron Collider.*, New Journal of Physics, 2006
- [9] Mariusz Sapinski, *LS1 CryoBLM installation notes*, EDMS-1342256, CERN, 2013
- [10] R. M. Sternheimer, *The Density Effect for the Ionization Loss in Various Materials*, *Phys. Rev.* **88**, 851, 1952
- [11] ICRU Report 49, *Stopping Powers and Ranges for Protons and Alpha Particles*, 1993

## BIBLIOGRAPHY

---

- [12] H.H Andersen, J.F Ziegler, *Hydrogen: Stopping Powers and Ranges in All Elements*, Vol. 3 of *The Stopping and Ranges of Ions in Matter*, Permamon Press, 1977
- [13] Landau Distribution, "[https://en.wikipedia.org/wiki/Landau\\_distribution](https://en.wikipedia.org/wiki/Landau_distribution)"
- [14] Landau Distribution, *Stefano Meroli*, "<http://meroli.web.cern.ch/meroli/>"
- [15] Misiakos K, Tsamakis D. , *Accurate measurements of the silicon intrinsic carrier density from 78 to 340 K.*, Journal of Applied Physics, 1993
- [16] Z. Li, H. Kraner, *Modelling and simulation of charge collection properties for neutron irradiated silicon detectors*, Nuclear Physics B - Proceedings Supplements 32, 398-409, 1993
- [17] L.J Beattie et al., *The electric field in irradiated silicon detectors*, Nuclear Instruments and Methods in Physics Research A 418, 314-321, 1998
- [18] R.S Sussmann, *CVD diamond for electronic devices and sensors*, John Wiley & Sons, Chichester, 2009
- [19] Ioffe Institute, Electronic Archive, New Semiconductor Materials. Characteristics & Properties, "<http://www.ioffe.ru/SVA/NSM/>"
- [20] Shockley, W., *Currents to Conductors Induced by a Moving Point Charge*, Journal of Applied Physics 9 (10): 635, 1938
- [21] Ramo, S., *emphCurrents Induced by Electron Motion*, Proceedings of the IRE 27, 1939
- [22] Zhong He, *Review of the Shockley–Ramo theorem and its application in semiconductor gamma-ray detectors*, Nuclear Instruments and Methods in Physics Research A 463, 250–267, 2001
- [23] Michael Moll, *Radiation Damage in Silicon Particle Detectors*, Hamburg, 2009
- [24] H. Spieler *SLUO Lecture # 6: Silicon Detectors*, "[http://www-group.slac.stanford.edu/sluc/lectures/detector\\_lecture\\_files/detectorlectures\\_6.pdf](http://www-group.slac.stanford.edu/sluc/lectures/detector_lecture_files/detectorlectures_6.pdf)", 1998
- [25] Particle Data Group, *Passage of particles through matter*, "<http://pdg.lbl.gov/2014/reviews/rpp2014-rev-passage-particles-matter.pdf>"

- [26] Particle Data Group, *Particle Detectors*, ”<http://pdg.lbl.gov/2014/reviews/rpp2014-rev-particle-detectors-accel.pdf>”
- [27] Daniela Bortoletto, *Detectors for Particle Physics: Semiconductor Detectors*, ”<https://indico.cern.ch/event/318530/>”, CERN Summer Student Courses, 2014
- [28] Julian Becker, *Signal Development in Silicon Sensors used for Radiation Detection*, Hamburg, 2010
- [29] Hendrik Jansen *Chemical Vapour Deposition Diamond: Charge Carrier Movement at Low Temperatures and Use in Time-Critical Applications* Genf/Bonn, 2013
- [30] Maria Maksimow, *Transient Current Technique (TCT) Characterization of Silicon Particle Detectors*, Espoo, 2009
- [31] University at Buffalo, *Poisson’s Equation and Relaxation Methods*, ”<http://www.physics.buffalo.edu/phy410-505/2011/topic3/app1/index.html>”
- [32] SRIM: Stopping Range of Ions in Matter, <http://www.srim.org/>
- [33] PV Education. org, *Optical Properties of Silicon*, ”<http://www.pveducation.org/pvcdrom/materials/optical-properties-of-silicon>”
- [34] *Handbook of Optical Constants of Solids*, Academic Press, 1985
- [35] Bernadette Kolbinger, *Weightfield: Simulation of a Silicon-Strip Detector*, HEPHY, 2012
- [36] WeightField2, <http://personalpages.to.infn.it/~cartigli/Weightfield2/Main.html>
- [37] Pablo de Castro, *TRACS : Transient Current Simulator*, <https://github.com/IFCA-HEP/TRACS>, RD50 Workshop, Geneve, CERN, 2014
- [38] CERN: Secondary Beams & Areas, *PS East Area*, ”<http://sba.web.cern.ch/sba/BeamsAndAreas/East/East.htm>”
- [39] Lau Gatignon, *Beam Properties for the East Area Irradiation Facility in the T8 Beam Line*, CERN, Engineering Department
- [40] Maciej Kwiatkowski et al, *Development of a beam loss measurement system with Gigabit Ethernet readout at CERN*, CERN-ACC-2013-0249, CERN, Geneve, 2012.

## BIBLIOGRAPHY

---

- [41] Maciej Kwiatkowski, *BLEDP Card communication protocol over Gigabit Ethernet link*, CERN, Geneve, 2015
- [42] Maciej Kwiatkowski et al, *A Real FPGA based Algorithm for the combination of Beam Loss Acquisition Methods used for the Measurement Dynamic Range Expansion*, CERN-ACC-2013-0250, CERN, Geneve, 2012
- [43] William Vigano et al, *10 Orders of Magnitude Current Measurement Digitisers for the CERN Beam Loss Systems*, CERN-ACC-2014-0001, CERN, Geneve, 2012
- [44] Christos Zamantzas et al, *System Architecture for measuring and monitoring Beam Losses in the Injector Complex at CERN*, CERN-ACC-2013-0252, CERN, Geneve, 2012
- [45] Maurice Glaser et al, *Dosimetry Assessments in the Irradiation Facilities at the CERN-PS Accelerator*, IEEE TRANSACTIONS ON NUCLEAR SCIENCE, VOL. 53, NO. 4, AUGUST 2006
- [46] Elena Verbitskaya et al, *CERN-RD39 collaboration activities aimed at cryogenic silicon detector application in High-Luminosity Large Hadron Collider*, NIMA 13th Pisa Meeting, 2015